Searches for Supersymmetry using the α_T variable with the CMS detector at the LHC

Darren Burton

Imperial College London
Department of Physics

A thesis submitted to Imperial College London
for the degree of Doctor of Philosophy

Abstract

Declaration

I, the author of this thesis, declare that the work presented within this document to be my own. The work presented in Chapters 3.4.1, 4 and 5 is a result of the authors own work or that of which I have been a major contributor unless explicitly stated otherwise, and is carried out within the context of the Imperial College London and CERN SUSY groups, itself a subsection of the greater CMS collaboration. All figures and studies taken from external sources are referenced appropriately throughout this document.

Darren Burton

Acknowledgements

Of the many people who deserve thanks, some are particularly prominent....

Preface

Contents

List of Figures

List of Tables

"The Universe is about 1,000,000 years old."
— Matthew Kenzie, 1987-present : Discoverer of the Higgs Boson.

Chapter 1.

Introduction

During the 20th century great advances have been made in our understanding of the universe, where it comes from, where it is going and what it is made of. The Standard Model (SM) first formulated in the 1960's is one of the crowning achievements in science's quest to explain the most fundamental processes and interactions that make up our universe. It has provided a highly successful explanation of a wide range of phenomena in Particle Physics and has stood up to extensive experimental scrutiny [1].

Despite it's successes it is not a complete theory, with significant questions remaining unanswered. It describes only three of the four known forces with gravity not incoorporated within the framework of the SM. Cosmological experiments infer that just $\sim 4\%$ of the observable universe exists as matter, with elusive "Dark Matter" accounting for a further $\sim 23\%$ [2]. However no particle predicted by the SM is able to account for it. At higher energy scales and small distances the (non-)unification of the fundamental forces point to problems with the SM at least at higher energies not yet probed experimentally.

Many theories exist as extensions to the SM and predict a range of observables that can be detected at the Large Hadron Collider (LHC) of which SUperSYmmetry (SUSY) is one such example. It predicts a new symmetry of nature in which all current particles in the SM would have a corresponding supersymmetric partner. Common to most Supersymmetric theories is a stable, weakly interacting Lightest Supersymmetric Partner (LSP), which has the properties of a possible dark matter candidate. The SM and the main principles of Supersymmetric theories are outlined in Chapter 2, with emphasis on placed on how experimental signatures of SUSY may reveal themselves at the LHC.

The experimental goal of the LHC is to further test the framework of the SM, exploring the TeV mass scale for the first time, and to seek a connection between the particles produced in proton collisions and dark matter. The first new discovery by this extraordinary machine was announced on the 4th of July 2012. The long-awaited discovery was the culmination decades of experimental endeavours in the search for the Higgs boson, providing an answer to the mechanism of electroweak symmetry breaking within the SM [3][4].

This discovery was made possible through data taken by the two multi purpose detectors (CMS and A Toroidal LHC ApparatuS (ATLAS)) located on the LHC ring. An experimental description of the CMS detector and the LHC is described in Chapter 3, including some of the object reconstruction used by CMS in searches for SUSY signatures. The performance of the CMS Level-1 calorimeter trigger, benchmarked by the author is also included within this chapter.

The analysis conducted by the author is detailed within Chapter 4. This chapter contains a description of the search for evidence of the production of Supersymmetric particles at the LHC. The main basis of the search centres around the kinematic dimensionless α_T variable, which provides strong rejection of backgrounds with fake missing energy signatures whilst maintaining good sensitivity to a variety of SUSY topologies. The author's work as an integral part of the analysis group is documented in detail, which has culminated in numerous publications over the past two years. The latest of which was published in the European Physical Journal C (EPJC) [5] and contains the results which are discussed within this and the sequential Chapter.

The author in particular has played a major role in the extension of the α_T analysis into the additional b-tagged and jet multiplicity dimensions increasing the sensitivity of the analysis to a range of SUSY topologies. Additionally the author has worked extensively in both increasing the statistical precision of electroweak predictions measured from simulation through analytical techniques, and the derivation of a data driven systematic uncertainty through the establishment of closure tests within the control samples of the analysis.

Also included within this Chapter is a method to search for SUSY signatures which are rich in top and bottom flavoured jet final states. A parametrisation of the b-tagging distribution for different Electroweak processes is used to establish templates, which are then used to estimate the expected number of 3 or 4 b-tagged jet events from SM

processes. The α_T search is used as a cross check for this template method to establish it's functionality.

Finally the interpretation of such results within the framework of a variety of Simplified Model Spectra (SMS), which describe an array of possible SUSY event topologies is documented in Chapter 5. A description of the statistical model used to derive these interpretations and the possible implications of the results presented in this thesis is discussed within this Chapter. Natural units are used throughout this thesis in which $\hbar$ = c = 1.

Chapter 2.

A Theoretical Overview

Within this chapter, a brief introduction and background to the SM is given. Its success as a rigorously tested and widely accepted theory is discussed as well as the deficiencies with this theory that hint there this theory is not a complete description of our universe. The motivations for new physics at the TeV scale and in particular Supersymmetric theories are outlined within Section (2.3), with the chapter concluding with how an experimental signature of such theories can be produced and observed at the LHC, Section (2.4).

2.1. The Standard Model

The SM is the name given to the relativistic Quantum Field Theory (QFT), where particles are represented as excitations of fields, which describes the interactions and properties of all the known elementary particles [6][7][8][9]. It is a renormalisable field theory which contains three symmetries: $SU(3)$ for colour charge, SU(2) for weak isospin and U(1) relating to weak hyper charge, which require its Lagrangian $\mathcal{L}_{SM}$ to be invariant under local gauge transformation.

Within the SM theory, matter is composed of spin $\frac{1}{2}$ fermions, which interact with each other via the exchange of spin-1 gauge bosons. A summary of the known fundamental fermions and bosons is given in Table 2.1.

Fermions are separated into quarks and leptons of which only quarks interact with the strong nuclear force. Quarks unlike leptons are not seen as free particles in nature, but rather exist only within baryons, composed of three quarks with an overall integer

5

Particle	Symbol	Spin	Charge	Mass (GeV)
First Generation Fermions				
Electron Neutrino	ν_e	$\frac{1}{2}$	0	$< 2.2 \times 10^{-6}$
Electron	e	$\frac{1}{2}$	-1	0.51×10^{-3}
Up Quark	u	$\frac{1}{2}$	$\frac{2}{3}$	$2.3^{+0.7}_{-0.5} \times 10^{-3}$
Down Quark	d	$\frac{1}{2}$	$-\frac{1}{3}$	$4.8^{+0.7}_{-0.3} \times 10^{-3}$
Second Generation Fermions				
Muon Neutrino	ν_μ	$\frac{1}{2}$	0	-
Muon	μ	$\frac{1}{2}$	-1	1.05×10^{-3}
Charm Quark	c	$\frac{1}{2}$	$\frac{2}{3}$	1.275 ± 0.025
Strange Quark	s	$\frac{1}{2}$	$-\frac{1}{3}$	$95 \pm 5 \times 10^{-3}$
Third Generation Fermions				
Tau Neutrino	ν_τ	$\frac{1}{2}$	0	-
Tau	τ	$\frac{1}{2}$	-1	1.77
Top Quark	t	$\frac{1}{2}$	$\frac{2}{3}$	173.5 ± 0.8
Bottom Quark	b	$\frac{1}{2}$	$-\frac{1}{3}$	4.65 ± 0.03
Gauge Bosons				
Photon	γ	1	0	0
W Boson	$W^\pm$	1	± 1	80.385 ± 0.015
Z Boson	Z	1	0	91.187 ± 0.002
Gluons	g	1	0	0
Higgs Boson	H	0	0	125.3 ± 0.5 [4]

Table 2.1.: The fundamental particles of the SM, with spin, charge and mass displayed. Latest mass measurements taken from [1].

charge, and quark-anti-quark pairs called mesons. Both leptons and quarks are grouped into three generations which have the same properties, but with ascending mass in each subsequent generation.

The gauge bosons mediate the interactions between fermions. The field theories of Quantum Electro-Dynamics (QED) and Quantum Chromo-Dynamics (QCD), yield massless mediator bosons, the photon and eight coloured gluons which are consequences of the gauge invariance of those theories, detailed in Section (2.1.1).

The unification of the electromagnetic and weak-nuclear forces into the current Electroweak theory yield the weak gauge bosons, $W^\pm$ and Z through the mixing of the associated gauge fields. The force carriers of this theory were experimentally detected by

the observation of weak neutral current, discovered in 1973 in the Gargamelle bubble chamber located at European Organization for Nuclear Research (CERN) [10], with the masses of and the weak gauge bosons measured by the UA1 and U2 experiments at the Super Proton Synchrotron (SPS) collider in 1983 [11][12].

2.1.1. Gauge Symmetries of the SM

Symmetries are of fundamental importance in the description of physical phenomena. Noether's theorem states that for a dynamical system, the consequence of any symmetry is an associated conserved quantity [13]. Invariance under translations, rotations, and Lorentz transformations in physical systems lead to conservation of momentum, energy and angular momentum.

In the SM, a quantum theory described by Lagrangian formalism, the weak,strong and electromagnetic interactions are described in terms of "gauge theories". A gauge theory possesses invariance under a set of "local transformations", which are transformations whose parameters are space-time dependent. The requirement of gauge invariance within the SM necessitates the introduction of force-mediating gauge bosons and interactions between fermions and the bosons themselves. Given the nature of the topics covered by this thesis, the formulation of Electroweak Sector (EWK) within the SM Lagrangian is reviewed within this section.

The simplest example of the application of the principle of local gauge invariance within the SM is in Quantum Electro-Dynamics (QED), the consequences of which require a massless photon field [14][15].

Starting from the free Dirac Lagrangian written as

$$\mathcal{L} = \bar{\psi}(i\gamma^\mu \partial_\mu - m)\psi, \tag{2.1}$$

where ψ represents a free non interacting fermionic field, with the matrices $\gamma^\mu, \mu \in 0, 1, 2, 3$ defined by the anti commutator relationship $\gamma^\mu\gamma^\nu + \gamma^\mu\gamma^\nu = 2\eta^{\mu\nu}I_4$ where $\eta^{\mu\nu}$ is the flat space-time metric $(+, -, -, -)$ and I_4 is the 4×4 identity matrix.

Under a local U(1) abelian gauge transformation in which ψ transforms as:

$$\psi(x) \rightarrow \psi^{'}(x) = e^{i\theta(x)}\psi(x) \qquad \bar{\psi}(x) \rightarrow \bar{\psi}^{'}(x) = e^{i\theta(x)}\bar{\psi}(x) \tag{2.2}$$

the kinetic term of the Lagrangian does not remain invariant, due to the partial derivative interposed between the $\bar{\psi}$ and ψ yielding,

$$\partial_\mu \psi \rightarrow e^{i\theta(x)}\partial_\mu \psi + ie^{i\theta(x)}\psi\partial_\mu\theta. \tag{2.3}$$

To ensure that $\mathcal{L}$ remains invariant, a modified derivative, D_μ, that transforms covariantly under phase transformations is introduced. In doing this a vector field A_μ with transformation properties that cancel out the unwanted term in (2.3) must also be included,

$$D_\mu \equiv \partial_\mu - ieA_\mu, \qquad A_\mu \rightarrow A_\mu + \frac{1}{e}\partial_\mu\theta. \tag{2.4}$$

Invariance of the Lagrangian is then achieved by replacing ∂_μ by D_μ:

$$\begin{aligned}
\mathcal{L} &= i\bar{\psi}\gamma^\mu D_\mu\psi - m\bar{\psi}\psi \\
&= \bar{\psi}(i\gamma^\mu\partial_\mu - m)\psi + e\bar{\psi}\gamma^\mu\psi A_\mu
\end{aligned} \tag{2.5}$$

An additional interaction term is now present in the Lagrangian, coupling the Dirac particle to this vector field, which is interpreted as the photon in QED. To regard this new field as the physical photon field, a term corresponding to its kinetic energy must be added to the Lagrangian from Equation (2.5). Since this term must also be invariant under the conditions of Equation (2.4), it is defined in the form $F_{\mu\nu} = \partial^\mu A^\nu - \partial_\nu A\mu$.

This then leads to the Lagrangian of QED:

$$\mathcal{L}_{QED} = .\overbrace{i\bar{\psi}\gamma^\mu\partial_\mu\psi - \frac{1}{4}F_{\mu\nu}F^{\mu\nu}}^{\text{kinetic term}} + \overbrace{m\bar{\psi}\psi}^{\text{mass term}} + \overbrace{e\bar{\psi}\gamma^\mu\psi A_\mu}^{\text{interaction term}} \qquad (2.6)$$

Within the Lagrangian there remains no mass term of the form $m^2 A_\mu A^\mu$, which is prohibited by gauge invariance. This implies that the gauge particle, the photon, must be massless.

2.1.2. The Electroweak Sector and Electroweak Symmetry Breaking

The same application of gauge symmetry and the requirement of local gauge invariance can be used to unify QED and the Weak force in the Electroweak Sector (EWK). The nature of EWK interactions is encompassed within a Lagrangian invariant under transformations of the group $SU(2)_L \times U(1)_Y$.

The weak interactions from experimental observation [16], are known to violate parity and are therefore not symmetric under interchange of left and right helicity fermions. Thus within the SM the left and right handed parts of these fermion fields are treated separately. A fermion field is then split into two left and right handed chiral components, $\psi = \psi_L + \psi_R$, where $\psi_{L/R} = (1 \pm \gamma^5)\psi$.

The $SU(2)_L$ group is the special unitary group of 2×2 matrices U satisfying $UU^\dagger = I$ and $det(U) = 1$. It may be written in the form $U = e^{-i\omega_i T_i}$, with the generators of the group $T_i = \frac{1}{2}\tau_i$ where τ_i, $i \in 1,2,3$ being the 2×2 Pauli matrices

$$\tau_1 = \begin{pmatrix} 0 & 1 \\ 1 & 0 \end{pmatrix} \qquad \tau_2 = \begin{pmatrix} 0 & -i \\ i & 0 \end{pmatrix} \qquad \tau_3 = \begin{pmatrix} 1 & 0 \\ 0 & -1 \end{pmatrix}, \qquad (2.7)$$

which form a non Abelian group obeying the commutation relation $[T^a, T^b] \equiv if^{abc}T^c \neq 0$. The gauge fields that accompany this group are represented by $\hat{W}_\mu = (\hat{W}_\mu^1, \hat{W}_\mu^2, \hat{W}_\mu^3)$ and act only on the left handed component of the fermion field ψ_L.

One additional generator Y which represents the hypercharge of the particle under consideration is introduced through the $U(1)_Y$ group acting on both components of the fermion field, with an associated vector boson field $\hat{B}_\mu$.

The $SU(2)_L \times U(1)_Y$ transformations of the left and right handed components of ψ are summarised by,

$$\chi_L \to \chi_L^{'} = e^{i\theta(x) \cdot T + i\theta(x)Y}\chi_L,$$
$$\psi_R \to \psi_R^{'} = e^{i\theta(x)Y}\psi_R, \tag{2.8}$$

where the left handed fermions form isospin doubles χ_L and the right handed fermions are isosinglets ψ_R. For the first generation of leptons and quarks this represents

$$\chi_L = \begin{pmatrix} \nu_e \\ e \end{pmatrix}_L, \qquad \begin{pmatrix} u \\ d \end{pmatrix}_L$$
$$\psi_R = e_R, \qquad\qquad u_R, d_R \tag{2.9}$$

Imposing local gauge invariance within $\mathcal{L}_{EWK}$ is once again achieved by modifying the covariant derivative

$$D_\mu = \partial_\mu - \frac{ig}{2}\tau^i W_\mu^i - \frac{ig^{'}}{2}Y B_\mu, \tag{2.10}$$

where g and $g^{'}$ are the coupling constant of the $SU(2)_L$ and $U(1)_Y$ groups respectively. Taking the example of the first generation of fermions defined in Equation.(2.9), with input hypercharge values of -1 and -2 for χ_L and e_R respectively, would lead to a Lagrangian $\mathcal{L}_1$ of the form,

$$\mathcal{L}_1 = \bar{\chi}_L\gamma^\mu[i\partial_\mu - g\frac{1}{2}\tau \cdot W_\mu - g^{'}(-\frac{1}{2})B_\mu]\chi_L$$
$$+ \bar{e}_R\gamma^\mu[i\partial_\mu - g^{'}(-1)B_\mu]e_R - \frac{1}{4}W_{\mu\nu} \cdot W^{\mu\nu} - \frac{1}{4}B_{\mu\nu}B^{\mu\nu}. \tag{2.11}$$

As in QED, these additional gauge fields introduce field strength tensors $B_{\mu\nu}$ and $W_{\mu\nu}$,

$$\hat{B}_{\mu\nu} = \partial_\mu \hat{B}_\nu - \partial_\nu \hat{B}_\mu \tag{2.12}$$

$$\hat{W}_{\mu\nu} = \partial_\mu \hat{W}_\nu - \partial_\nu \hat{W}_\mu - g\hat{W}_\mu \times \hat{W}_\mu \tag{2.13}$$

corresponding to the kinetic energy and self coupling of the W_μ fields and the kinetic energy term of the B_μ field.

None of these gauge bosons are physical particles, and instead linear combinations of these gauge bosons make up γ and the W and Z bosons, defined as

$$W^\pm = \frac{1}{\sqrt{2}}\left(W_\mu^1 \mp iW_\mu^2\right) \qquad \begin{pmatrix} Z_\mu \\ A_\mu \end{pmatrix} = \begin{pmatrix} cos\theta_W & -sin\theta_W \\ sin\theta_W & cos\theta_W \end{pmatrix} \begin{pmatrix} W_\mu^3 \\ B_\mu \end{pmatrix} \tag{2.14}$$

where the mixing angle, $\theta_w = \tan^{-1}\frac{g'}{g}$, relates the coupling of the neutral weak and electromagnetic interactions.

As in the case of the formulation of the QED Lagrangian there remains no mass term for the photon. However this is also the case for the W, Z and fermions in the Lagranian, contrary to experimental measurement. Any explicit introduction of mass terms would break the symmetry of the Lagrangian and instead mass terms can be introduced through spontaneous breaking of the EWK symmetry via the Higgs mechanism.

The Higgs mechanism induces spontaneous symmetry breaking through the introduction of a complex scalar SU(2) doublet field ϕ which attains a non-zero Vacuum Expectation Value (VEV) [17][18][19][20].

$$\phi = \begin{pmatrix} \phi^+ \\ \phi^0 \end{pmatrix} \qquad with \qquad \begin{aligned} \phi^+ &\equiv (\phi_1 + i\phi_2)/\sqrt{2} \\ \phi^0 &\equiv (\phi_3 + i\phi_4)/\sqrt{2} \end{aligned} \tag{2.15}$$

328   The Lagrangian defined in Equation (2.11) attains an additional term $\mathcal{L}_{Higgs}$ of the
329 form

$$
\mathcal{L}_{Higgs} = \overbrace{(D_\mu \phi)^\dagger (D^\mu \phi)}^{\text{kinetic}} - \overbrace{\mu^2 \phi^\dagger \phi - \lambda (\phi^\dagger \phi)^2}^{\text{potential V}(\phi)} \qquad (\mu^2, \lambda) > 0 \in \mathbb{R},
$$
$$
\mathcal{L}_{SM} = \mathcal{L}_{EWK} + \mathcal{L}_{Higgs}, \tag{2.16}
$$

330   where the covariant derivative D_μ is that defined in Equation (2.10). The last two
331 terms of $\mathcal{L}_{Higgs}$ correspond to the Higgs potential, in which positive real positive values
332 of μ^2 and λ are required to ensure the generation of masses for the bosons and leptons.
333 The minimum of this potential is found at $\phi^\dagger \phi = \frac{1}{2}(\phi_1^2 + \phi_2^2 + \phi_3^2 + \phi_4^2) = \mu^2/\lambda = v^2$,
334 where v represents the VEV.

335   Defining the ground state of the ϕ field to be consistent with the $V(\phi)$ minimum, and
336 then expanding around a ground state chosen to maintain an unbroken electromagnetic
337 symmetry thus preserving a zero photon mass [21] leads to

$$
\phi_0 = \sqrt{\frac{1}{2}} \begin{pmatrix} 0 \\ v \end{pmatrix}, \qquad \phi(x) = e^{i\tau \cdot \theta(x)/v} \sqrt{\frac{1}{2}} \begin{pmatrix} 0 \\ v + h(x) \end{pmatrix}, \tag{2.17}
$$

338   where the fluctuations from the vacuum ϕ_0 are parametrized in terms of four real
339 fields, $\theta_1, \theta_2, \theta_3$ and $h(x)$.

340   Choosing to gauge away the three massless Goldstone boson fields by setting $\theta(x)$ to
341 zero and subsituting $\phi(x)$ back into kinetic term of $\mathcal{L}_{Higgs}$ from Equation (2.16) leads to
342 mass terms for the $W^\pm$ and Z bosons

$$
(D_\mu \phi)^\dagger (D^\mu \phi) = \frac{1}{2}(\partial_\mu h)^2 + \frac{g^2 v^2}{2} W_\mu^+ W^{-\mu} + \frac{v^2 g^2}{8 \cos^2 \theta_w} Z_\mu Z^\mu + 0 A_\mu A^\mu, \tag{2.18}
$$

343   where the relations between the physical and electroweak gauge fields from Equation
344 (2.14) are used. The $W^\pm$ and Z bosons can then be determined to be

$$M_W = \frac{1}{2}gv \qquad M_Z = \frac{1}{2}\frac{gv}{\cos\theta_w}. \tag{2.19}$$

This mechanism is also used to generate fermion masses by introducing a Yukawa coupling between the fermions and the ϕ field [22], with the coupling strength of a particle to the ϕ field governing its mass. Additionally a scalar boson h with mass $m_h = v\sqrt{\frac{\lambda}{2}}$, is also predicted as a result of this spontaneous symmetry breaking and became known as the Higgs boson. Its discovery by the CMS and ATLAS experiments in 2012 is concrete evidence to support this method of mass generation within the SM.

2.2. Motivation for Physics Beyond the Standard Model

As has been described, the SM has proved to be a very successful theory, predicting the existence of the $W^{\pm}$ and Z bosons and the top quark long before they were experimentally observed. However the theory does not accurately describe all observed phenomena and has some fundamental theoretical flaws that hint at the need for additional extensions to the current theory.

On a theoretical level, the SM is unable to incorporate the gravitational interactions of fundamental particles within the theory. Whilst at the electroweak energy scales the relative strength of gravity is negligible compared to the other three fundamental forces, at much higher energy scales $M_{planck} \sim 10^{18} GeV$ quantum gravitational effects become increasingly dominant. The failure to reconcile gravity within the SM, demonstrates that the SM must become invalid at some higher energy scale.

Some other deficiencies with the SM include the fact that the predicted rate of Charge-Parity violation does not account for the matter dominated universe which we inhabit, and the SM prediction of zero neutrino mass conflicts with the observation of neutrino flavour mixing, attributed to mixing between neutrino mass eigenstates [23][24].

Perhaps one of the most glaring gaps in the predictive power of the SM is that there exists no candidate to explain the cosmic dark matter observed in galactic structures through indirect techniques including gravitational lensing and measurement of the orbital velocity of stars in galactic edges. Any such candidate must be very weakly

$_{372}$ interacting which must also be stable, owing to the lack of direct detection of the decay
$_{373}$ products of such an process. Providing a dark matter candidate is of the prime goals
$_{374}$ which be tackled by any Beyond Standard Model (BSM) physics model.

$_{375}$ The recent discovery of the Higgs boson whilst a significant victory for the predictive
$_{376}$ power of the SM, brings with it still unresolved questions. This issue is commonly
$_{377}$ described as the "hierarchy problem".

$_{378}$ In the absence of new physics between the TeV and Planck scale, calculating beyond
$_{379}$ tree-level contributions to the Higgs mass term given by its self interaction, result in
$_{380}$ divergent terms that push the Higgs mass up to the planck mass M_{planck}.
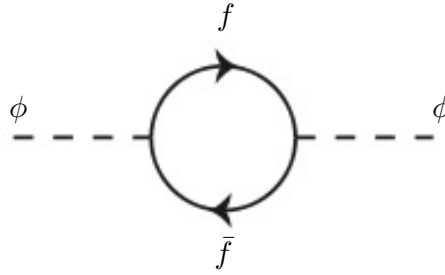
Figure 2.1.: One loop quantum corrections to the Higgs squared mass parameter m_h^2 due to
a fermion.

$_{381}$ This can be demonstrated by considering the one loop quantum correction to the
$_{382}$ Higgs mass with a fermion f, shown in Figure 2.1 with mass m_f. The Higgs field couples
$_{383}$ to f with a term in the Lagrangian $-\lambda_f h \bar{f} f$, yielding a correction of the form [25],

$$\delta m_h^2 = -\frac{|\lambda_f|^2}{8\pi^2}\Lambda^2 + .., \tag{2.20}$$

$_{384}$ where λ_f represents the coupling strength for each type of fermion $\propto m_f$, and Λ the
$_{385}$ cutoff energy scale at which the SM ceases to be a valid theory.

$_{386}$ To recover the mass of the now discovered Higgs boson would require a fine-tuning of
$_{387}$ the parameters to cancel out these mass corrections the the Higgs mass to the scale of
$_{388}$ 30 orders of magnitude. This appears as an unnatural solution to physicists and it is
$_{389}$ this hierarchy problem that provides one of the strongest motivations for the theory of
$_{390}$ SUperSYmmetry (SUSY).

2.3. Supersymmmetry Overview

Supersymmetry provides potential solutions to many of the issues raised in the previous section. It provides a dark matter candidate, can explain baryogenesis in the early universe and also provides an elegant solution to the hierarchy problem [26][27][28][29]. At it's heart it represents a new space-time symmetry that relates fermions and bosons. This symmetry converts bosonic states into fermionic states, and vice versa, see Equation (2.21) ,

$$Q|Boson\rangle = |Fermion\rangle \qquad Q|Fermion\rangle = |Boson\rangle, \qquad (2.21)$$

where the operator Q is the generator of these transformations. Quantum field theories which are invariant under such transformations are called supersymmetric.

This symmetry operator therefore acts upon a particles spin altering it by a half integer value. The consequences of the introduction of this additional space-time symmetry introduce a new rich phenomenology. For example in supersymmetric theories, both the left handed SU(2) doublet and right handed singlet of fermions will have a spin-0 superpartner, containing the same electric charge, weak isospin, and colour as its SM partner. In the case of the leptons $(\nu_l, l)_L$ will have two superpartners, a sneutrino $\widetilde{\nu}_{lL}$ and a slepton $\widetilde{l}_L$, whilst the single l_R also has a superpartner slepton $\widetilde{l}_R$.

Each particle in a supersymmetric theory is paired together with their superpartners as a result of this supersymmetric transformations in a so called supermultiplet. These superpartners will then consequently also contribute to the corrections to the Higgs mass. Bosonic and fermionic loops contributing to the correction appear with opposite signs, and therefore cancellation of these divergent terms will stabilise the Higgs mass, solving the hierarchy problem [30][31].

One of the simplest forms of SUSY would predict a whole set of supersymmetric partners to their SM counterparts with the same mass and interactions. However the currently lack of any experimental evidence for the predicted sparticle spectrum implies SUSY must be a broken symmetry in which any sparticle masses must be greater than their SM counterparts.

There exist many techniques which can induce supersymmetric breaking [32][33][34]. Of particular interest to experimental physicists are those at which the breaking scale

is of an order that is experimentally accessible to the LHC i.e. $\sim$ TeV scale. Whilst there is no requirement for supersymmetric breaking to occur at this energy scale, for supersymmetry to provide a solution to the hierarchy problem, it is necessary for this scale to not differ too drastically from the EWK scale [35][36].

2.3.1. R-Parity

Some supersymmetric theories also present a solution to the dark matter problem. Such theories can contain a Lightest Supersymmetric Partner (LSP), which matches the criteria of a Weakly Interacting Massive Particle (WIMP) required by cosmological observation if R-parity is conserved.

Baryon (B) and Lepton (L) number conservation is forbidden in the SM by renormalisability requirements. The violation of Baryon or Lepton number would result in the proton lifetime much shorter than those set by experimental limits [37]. Another symmetry called R-parity is then often introduced to SUSY theories to maintain baryon and lepton conservation.

R-parity is described by the equation

$$R_P = (-1)^{3(B-L)+2s},$$ (2.22)

where s represents the spin of the particles. $B = \pm\frac{1}{3}$ for quarks/antiquarks and $B = 0$ for all others, $L = \pm 1$ for leptons/antileptons, $L = 0$ for all others.

R-parity ensures the stability of the proton in SUSY models, and also has other consequences for the production and decay of supersymmetric particles. At particle colliders supersymmetric particles can only be pair produced, and similarly the decay of any produced supersymmetric particle is restricted to a SM particle and a lighter supersymmetric particle as allowed by conservation laws. A further implication of R-parity is that once a supersymmetric particle has decayed to the LSP it remains stable, unable to decay into a SM particle.

A LSP would not interact in a detector at a particle collider, leaving behind a missing energy $\not{E}_T$ signature. The assumption of R-parity and its consequences are used to determine the physical motivation and search strategies for SUSY model at the LHC.

2.4. Experimental signatures of SUSY at the LHC

Should strongly interacting sparticles be within the experimental reach of the LHC, then it is expected that they can be produced in a variety of ways.

- squark/anti-squark and gluino pairs can be produced via both gluon fusion and quark/anti-quark scattering.

- a gluino and squark produced together via quark-gluon scattering

- squark pairs produced via quark-quark scattering

Whilst most SUSY searches invoke the requirement of R-parity to explore parameter phase space, there still exist a whole plethora of possible SUSY model topologies which could be discovered at the LHC.

During the 2011 run period at a $\sqrt{s} = 7$ TeV particular models were used to benchmark performance and experimental reach of both CMS searches and previous experiments. The Compressed Minimal SuperSymmetric Model (CMSSM) was initially chosen for a number of reasons [38]. One of the most compelling being the reduction from the up to 105 new parameters introduced by SUSY in addition to the existing 19 of the SM to that of just 5 free extra free parameters. It was this simplicity, combined with the theory not requiring any fine tuning of particle masses to produce the experimentally verified SM that made it an attractive model to interpret physics results.

However recent results from the LHC now strongly disfavour large swathes of CMSSM parameter space [39][40][41]. In the face of such results a more pragmatic model independent search strategy is now applied across most SUSY searches at the LHC, see Section (2.4.1).

As previously stated, a stable LSP that exhibits the properties of a dark matter would be weakly interacting and therefore will not be directly detected in a detector environment. Additionally the cascade decays of supersymmetric particles to the LSP would also result in significant hadronic activity. These signatures can then be characterised through large amounts of hadronic jets (see Section (3.3.1)), leptons and a significant amount of missing energy dependent upon the size of the mass splitting between the LSP and the supersymmetric particle it has decayed from.

Whilst the SM contains processes which can exhibit a similar event topology to that described above. The largest contribution of which comes in from the general QCD

environment of a hadron collider. A multitude of different analytical techniques are used by experimental physicists to reduce or estimate any reducible or irreducible backgrounds, allowing a possible SUSY signature to be extracted. The techniques employed within this thesis are described in great detail within Section (4.1).

2.4.1. Simplified Models

With such a variety of different ways for a SUSY signal to manifest itself, it is necessary to be able to interpret experimental reach through the masses of gluinos and squarks which can excluded by experimental searches rather than on a model specific basis.

This is accomplished through SMS models, which are defined by a set of hypothetical particles and a sequence of their production and decay [42][43]. In the SMS models considered within this thesis, only the production process for the two primary particles are considered. Each primary particle can undergo a direct or a cascade decay through an intermediate new particle. At the end of each decay chain there remains a neutral, undetected LSP particle, denoted $\widetilde{\chi}_{LSP}$ which can represent a neutralino or gravitino. Essentially it is easier to consider each SMS with branching ratios set to 100% The masses of the primary particle and the LSP remain as free parameters, in which the absolute value and relative difference between the primary and LSP particle alter the kinematics of the event.

Different SMS models are denoted with a T-prefix, with a summary of the types interpreted within this thesis listed below [44].

- **T1,T1xxxx**, models represent a simplified version of gluino pair production with each gluino (superpartner to the gluon) undergoing a three-body decay to a quark-antiquark pair and the LSP (i.e. $\widetilde{g} \to q\bar{q}\widetilde{\chi}_{LSP}$). The resultant final state from this decay is typically 4 jets $+ \not{E}_T$ in the absence of initial/final state radiation and detector effects. xxxx denotes models in which the quarks are of a specific flavour, typically t or b quark-antiquarks.

- **T2,T2xx**, models represent a simplified version of squark anti-squark production with each squark undergoing a two-body decay into a light-flavour quark and LSP (i.e. $\widetilde{q} \to q\widetilde{\chi}_{LSP}$). This results in final states with less jets than gluino mediated production, typically 2 jets $+ \not{E}_T$ when again ignoring the effect of initial/final state radiation and detector effects. xx models again represent decays in which both the

509 quark and the squark within the decay is of a specific flavour, typically $\widetilde{t}/t$ or $\widetilde{b}/b$
510 flavoured.

511 Models rich in b and t quarks are interpreted within this thesis as they remain of
512 particular interest within "Natural SUSY" scenarios [45][46]. The largest contribution
513 to the quadratic divergence in the Higgs mass parameter comes from a loop of top
514 quarks via the Yukawa coupling. Cancellation of these divergences can be achieved in
515 supersymmetric theories by requiring a light right handed top squark, $\widetilde{t}_R$, and left-handed
516 double $SU(2)_L$ double containing top and bottom squarks, $(\frac{\widetilde{t}}{\widetilde{b}})_L$ [47].

517 These theories therefore solve the hierarchy problem by predicting light $\sim$ EWK
518 scale third generation sleptons, to be accessible at the LHC. Search strategies involving
519 the requirement of b-tagging (see Section (3.3.2) are used to give sensitivity to these
520 type of SUSY scenarios and are discussed in greater detail within Chapter 5.

521 Two example decay chains are shown in Figure 2.2; the pair production of gluinos
522 (T1) and the pair production of squarks (T2) decaying into SM particles and LSP's.
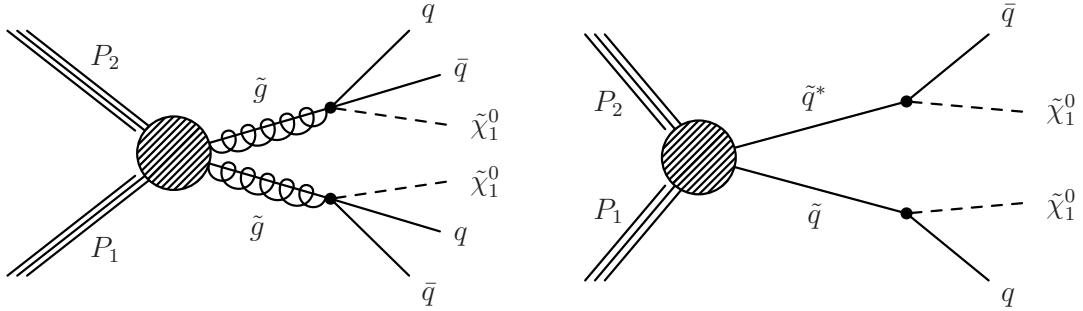
Figure 2.2.: Two example SMS model decays (T1 (left),T2 (right)), which are used in interpretations of physics reach by CMS.

Chapter 3.

The LHC and the CMS Detector

Probing the SM for signs of new physics would not be possible without the immensely complex electronics and machinery that makes the TeV energy scale accessible for the first time. This chapter will cover the LHC based at European Organization for Nuclear Research (CERN) and the Compact Muon Solenoid (CMS) detector, being the experiment the author is a member of. Section (3.2) serves to introduce an overview of the different components of the CMS detector, with more detail spent on those that are relevant in the search for Supersymmetric particles. Section (3.3) will focus on event and object reconstruction again with more emphasis on jet level quantities which are most relevant to the author's analysis research. Finally Section (3.4) will cover work performed by the author, as service to the CMS Collaboration, in measuring the performance of the Global Calorimeter Trigger (GCT) component of the L1 trigger during the 2012-2013 run period.

3.1. The LHC

The LHC is a storage ring, accelerator, and collider of circulating beams of protons or ions. Housed in the tunnel dug for the Large Electron-Positron collider (LEP), it is approximately 27 km in circumference, 100 m underground, and straddles the border between France and Switzerland outside of Geneva. It is currently the only collider in operation that is able to study physics at the TeV scale. A double-ring circular synchrotron, it was designed to collide both proton-proton (pp) and heavy ion (PbPb) with a centre of mass energy $\sqrt{s} = 14$ TeV at a final design luminosity of $10^{34} \mathrm{cm}^{-2}\mathrm{s}^{-1}$.

These counter-circulating beams of protons/Pb ions are merged in four sections around the ring to enable collisions of the beams, with each interaction point being home to one of the four major experiments; A Large Ion Collider Experiment (ALICE) [48] , A Toroidal LHC ApparatuS (ATLAS) [49], Compact Muon Solenoid (CMS) [50] and Large Hadron Collider Beauty (LHCb) [51] which record the resultant collisions. The layout of the LHC ring is shown in Figure 3.1. The remaining four sections contain acceleration,collimation and beam dump systems. In the eight arc sections, the beams are steered by magnetic fields of up to 8 T provided by super conduction dipole magnets, which are maintained at temperatures of 2 K using superfluid helium. Additional magnets for focusing and corrections are also present in straight sections within the arcs and near the interaction regions where the detectors are situated.
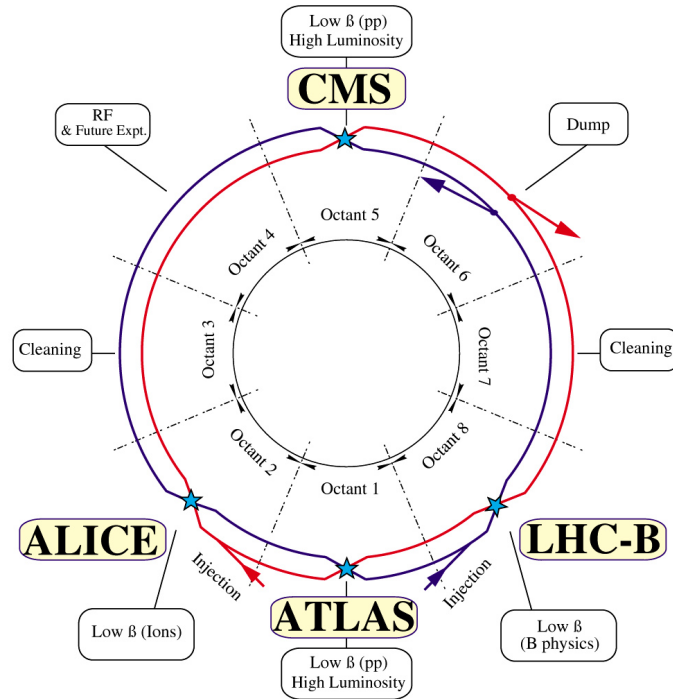
Figure 3.1.: A top down layout of the LHC. [52], with the position of the four main detectors labelled.

Proton beams are formed inside the Proton Synchrotron (PS) from bunches of protons 50 ns apart with an energy of 26 GeV. The protons are then accelerated in the Super Proton Synchrotron (SPS) to 450 GeV before being injected into the LHC. These LHC proton beams consists of many "bunches" i.e. approximately 1.1×10^{11} protons localized into less than 1 ns in the direction of motion. Before collision the beams are ramped to 4

TeV (2012) per beam in a process involving increasing the current passing through the dipole magnets. Once the desired $\sqrt{s}$ energy is reached then the beams are allowed to collide at the interaction points. The luminosity falls regularly as the run progresses as protons are lost in collisions, and eventually the beam is dumped before repeating the process again.

Colliding the beams produced an instantaneous luminosity of approximately 5×10^{33} cm^{-2}s^{-1} during the 2012 run. The high number of protons in each bunch increases the likelihood of multiple interactions with each crossing of the counter-circulating beams. This leads to isotropic energy depositions within the detectors positioned at these interaction points, increasing the energy scale of the underlying event. This is known as pile-up and the counteracting of it's effects are important to the many measurements performed at the LHC.

In the early phase of prolonged operation after the initial shutdown the machine operated in 2010-2011 at 3.5 TeV per beam, $\sqrt{s} = 7$ TeV, delivering 6.13 fb^{-1} of data [53]. During the 2012-2013 run period, data was collected at an increased $\sqrt{s} = 8$ TeV improving the sensitivity of searches for new physics. Over the whole run period 23.3 fb^{-1} of data was delivered of which 21.8 fb^{-1} was recorded by the CMS detector as shown in Figure 3.2 [53]. A total of 12 fb^{-1} of 8 TeV certified data was collected by October 2012, and it is this data which forms the basis of the results discussed within this thesis.
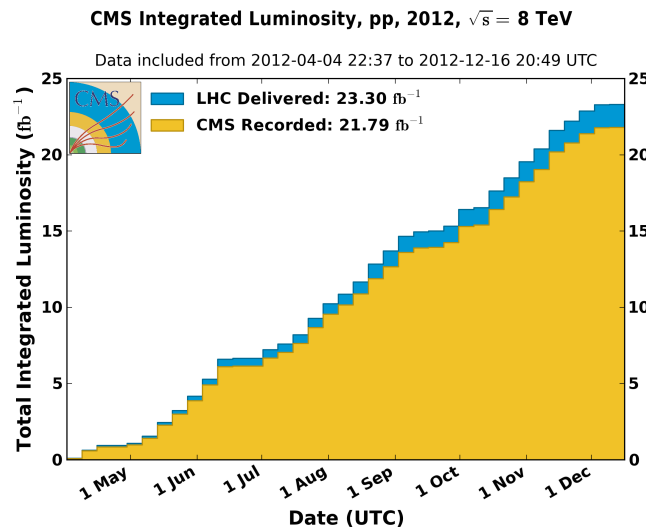

Figure 3.2.: The total integrated luminosity delivered to and collected by CMS during the 2012 8 TeV pp runs.

3.2. The CMS detector

The Compact Muon Solenoid (CMS) detector is one of two general purpose detectors at the LHC designed to search for new physics. The detector is designed to provide efficient identification and measurement of many physics objects including photons, electrons, muons, taus, and hadronic showers over wide ranges of transverse momentum and direction. Its nearly 4π coverage in solid angle allows for accurate measurement of global transverse momentum imbalance. These design factors give CMS the ability to search for direct production of SUSY particles at the TeV scale, making the search for Supersymmetric particles one of the highest priorities among the wide range of physics programmes at CMS.

CMS uses a right-handed Cartesian coordinate system with the origin at the interaction point and the z-axis pointing along the beam axis, the x-axis points radially inwards to the centre of the collider ring, with the y-axis points vertically upward. The azimuthal angle, ϕ ranging between $[-\pi,\pi]$ is defined in the x-y plane starting from the x-axis. The polar angle θ is measured from the z axis. The common convention in particle physics is to express an out going particle in terms of ϕ and its pseudorapidity defined as

$$\eta = -\log\tan\left(\frac{\theta}{2}\right). \tag{3.1}$$

The variable $\Delta R = \sqrt{\Delta\phi^2 + \Delta\eta^2}$ is commonly used to define angular distance between objects within the detector and additionally energy and momentum is typically measured in the transverse plane perpendicular to the beam line. These values are calculated from the x and y components of the object and are denoted as $E_T = E\sin\theta$ and $p_T = \sqrt{p_x^2 + p_y^2}$.

3.2.1. Detector Subsytems

As the range of particles produced in pp collisions interact in different ways with matter, CMS is divided into subdetector systems, which perform complementary roles to identify the identity, mass and momentum of the different physics objects present in each event. These detector sub-systems contained inside CMS are wrapped in layers

around a central 13 m long 4 T super conducting solenoid as shown in Figure 3.3. With the endcaps closed , CMS is a cylinder of length 22 m, diameter 15 m, and mass 12.5 kilotons. A more detailed complete description of the detector can be found elsewhere [50].
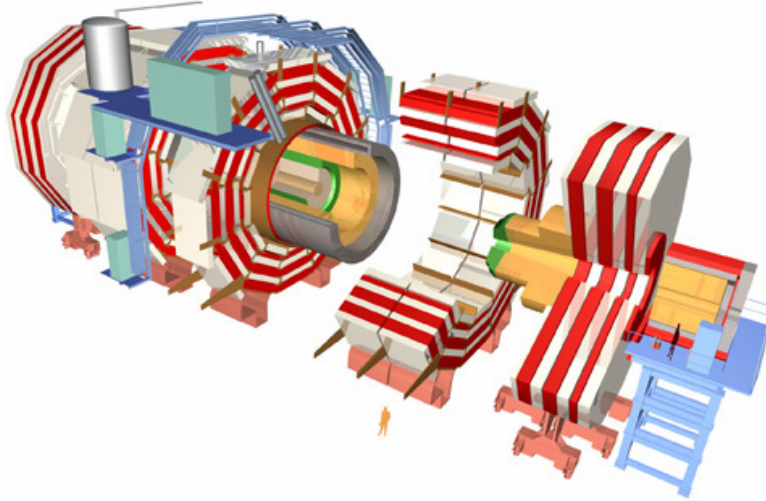
Figure 3.3.: A pictorial depiction of the CMS detector with the main detector subsystems labelled. [54]

3.2.2. Tracker

The inner-most subdetector of the barrel is the multi-layer silicon tracker, formed of a pixel detector component encased by layers of silicon strip detectors. The pixel detector consists of three layers of silicon pixel sensors providing measurements of the momentum, position coordinates of the charged particles as they pass, and the location of primary and secondary vertices between 4cm and 10cm transverse to the beam. Outside the pixel detector, ten cylindrical layers of silicon strip detectors extend the tracking system out to a radius of 1.20m from the beam line. The tracking system provides efficient and precise determination of the charges, momenta, and impact parameters of charged particles with the geometry of the tracker extending to cover a rapidity range up to $|\eta| < 2.5$.

The tracking system also plays a crucial part in the identification of jets originating from b-quarks through measurement of displaced secondary vertices, which is covered in more detail in Section (3.3.2). The identification of b-jets is important in many searches

for natural SUSY models and forms an important part of the inclusive search strategy described within Section (4.1.1).

3.2.3. Electromagnetic Calorimeter

Immediately outside of the tracker, but still within the magnet core, sits the Electromagnetic CALorimeter (ECAL). Covering a pseudorapididity up to $|\eta| < 3$ and compromising of over 75,000 $PbWO_4$ (lead tungstate) crystals that scintillate as particles deposit energy, the ECAL provides high resolution measurements of the electromagnetic showers from photons, electrons in the detector.

Lead tungstate is used because of its short radiation length ($X_0 \sim 0.9$cm) and small Molieré radius (~ 2.1cm) leading to high granularity and resolution. It's fast scintillation time (~ 25ns) reduces the effects of pile-up due to energy from previous collisions still being read out, and its radiation hardness gives it longevity. The crystals are arranged in modules which surround the beam line in a non-projective geometry, angled at $3°$ with respect to the interaction point to minimise the risk of particles escaping down the cracks between the crystals.

The ECAL is primarily composed of two sections, the Electromagnetic CALorimeter Barrel (EB) which extends in pseudo-rapidity to $|\eta| < 1.479$ with a crystal front cross section of 22 × 22 mm^2 and a length of 230 mm corresponding to 25.8 radiation lengths, and the Electromagnetic CALorimeter Endcap (EE) covering a rapidity range of $1.479 < |\eta| < 3.0$, which consists of two identical detectors on either side of the EB. A lead-silicon sampling 'pre-shower' detector Electromagnetic CALorimeter pre-Shower (ES) is placed before the endcaps to aid in the identification of neutral pions. Their arrangement are shown in Figure 3.4.

Scintillation photons from the lead tungstate crystals are instrumented with Avalanche Photo-Diodes (APD) and Vacuum Photo-Triodes (VPT) located in the EB and EE respectively, converting the scintillating light into an electric signal which is consequently used to determine the amount of energy deposited within the crystal . These instruments are chosen for their resistance under operation to the strong magnetic field of CMS. The scintillation of the ECAL crystals as well as the response of the APDs varies as a function
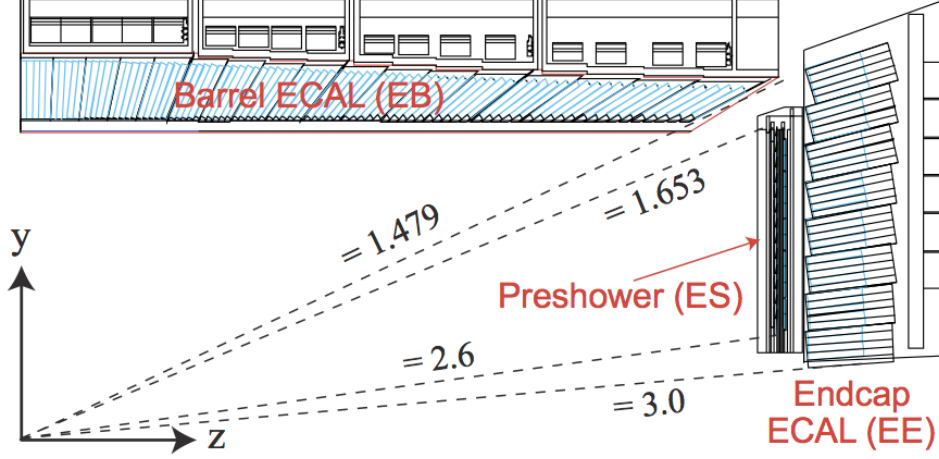
Figure 3.4.: Illustration of the CMS ECAL showing the arrangement of the lead tungstate crystals in the EB and EE. The ES is also shown and is located infront of the EE [55].

of temperature and so cooling systems continually maintain an overall constant ECAL temperature $\pm\, 0.05°C$.

3.2.4. Hadronic Calorimeter

Beyond the ECAL lies the Hadronic CALorimeter (HCAL) which is responsible for the accurate measurement of hadronic showers, crucial for analyses involving jets or missing energy signatures. The HCAL is a sampling calorimeter which consists of alternating layers of brass absorber and plastic scintillator, except in the hadron forward $(3.0 < |\eta| < 5.0)$ region in which steel absorbers and quartz fibre scintillators are used because of their increased radiation tolerance. Hadron showers are initiated in the absorber layers inducing scintillation in the plastic scintillator tiles. These scintillation photons are converted by wavelength shifting fibres for read-out by hybrid photodiodes.

The HCAL's size is constrained to a compact size by the presence of the solenoid, requiring the placement of an additional outer calorimeter on the outside of the solenoid to increase the sampling depth of the HCAL. A schematic of the HCAL can be seen in Figure 3.5.
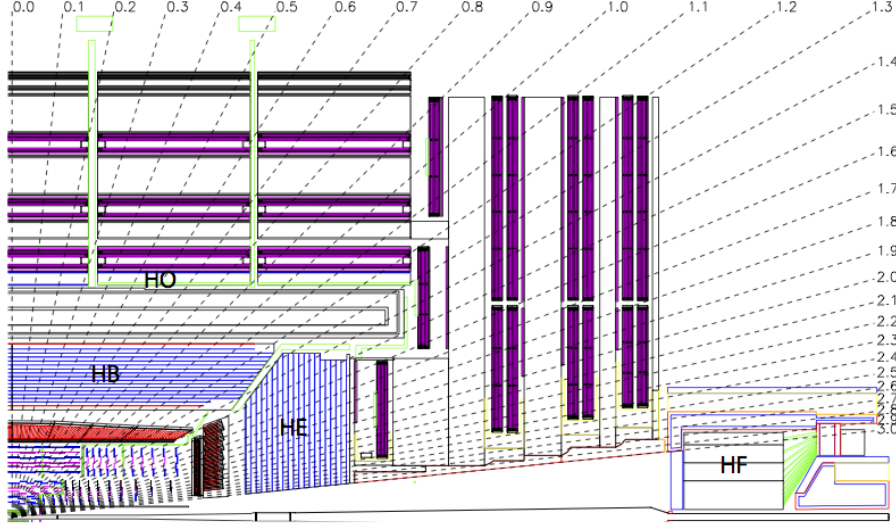
Figure 3.5.: Schematic of the hadron calorimeters in the r-z plane, showing the locations of the HCAL components and the HF. [50].

The HCAL covers the range $|\eta| < 5$ and consists of four subdetectors: the Hadron Barrel (HB) $|\eta| < 1.3$, the Hadron Outer (HO), the Hadron Endcaps (HE) $1.3 < |\eta| < 3.0$ and the Hadron Forward (HF). The HB is contained between the outer edge of the ECAL and the inner edge of the solenoid, formed of 36 azimuthal wedges it is split between two half-barrel segments. The relatively short number of interaction lengths (λ_l, the distance a hadron will travel through the absorber material before it has lost $\frac{1}{e}$ of its energy) within the HB, the lowest being $\lambda_l = 5.82$ for $|\eta| = 0$, facilitates the need for the 'tail catching' HO to increase the sampling depth in the central barrel rapidity region $|\eta| < 1.3$ to 11 interaction lengths . Significant fractions of the hadrons energy will be deposited in the ECAL as it passed through the detector. Therefore measurements of hadron energies in the central regions $|\eta| < 3.0$ use both the ECAL and HCAL to reconstruct the true energy from showering hadrons.

3.2.5. Muon Systems

Muons being too massive to radiate away energy via Bremsstrahlung, interact little in the calorimeters and mostly pass through the detector until they reach the system of muon detectors which forms the outer most part of the CMS detector.

⁶⁹² Outside of the superconducting solenoid are four muon detection layers interleaved
⁶⁹³ with the iron return yokes which measure the muons energy via ionisation of gas within
⁶⁹⁴ detector elements. Three types of gaseous chamber are used. The Drift Tube (DT),
⁶⁹⁵ Cathode Stripe Chamber (CSC), and Resistive Plate Chamber (RPC) systems provide
⁶⁹⁶ efficient detection of muons with pseudo-rapidity $|\eta| < 2.4$. The best reconstruction
⁶⁹⁷ performance is obtained when the muon chamber is combined with the inner tracking
⁶⁹⁸ information to determine muon trajectories and their momenta [56].
⁶⁹⁹

3.3. Event Reconstruction and Object Definition

⁷⁰¹ The goal of event reconstruction is to take the raw information recorded by the detector
⁷⁰² and to compute from it higher-level quantities which can be used at an analysis level.
⁷⁰³ These typically correspond to an individual particle's energy and momenta, or groups of
⁷⁰⁴ particles which shower in a narrow cone and the overall global energy and momentum
⁷⁰⁵ balance of the event. The reconstruction of these objects are described in great detail in
⁷⁰⁶ [57], however covered below are brief descriptions of those which are most relevant to the
⁷⁰⁷ analysis detailed in Section (4).

3.3.1. Jets

⁷⁰⁹ Quarks and gluons are produced copiously at the LHC in the hard scattering of partons.
⁷¹⁰ As these quarks and gluons fragment, they hadronise and decay into a group of strongly
⁷¹¹ interactive particles and their decay products. These streams of particles travel in the
⁷¹² same direction, as they have been "boosted" by the momentum of the primary hadron.
⁷¹³ These collections of decay products are reconstructed and identified together as a "jet".

⁷¹⁴ At CMS jets are reconstructed from energy deposits in the detector using the anti-kt
⁷¹⁵ algorithm [58] with size parameter $\Delta R = 0.5$. The anti-kt jet algorithm clusters jets by
⁷¹⁶ defining a distance between hard (high p_T) and soft (low p_T) particles such that soft
⁷¹⁷ particles are preferentially clustered with hard particles before being clustered between
⁷¹⁸ themselves. This produces jets which are robust to soft particle radiation from the pile-up
⁷¹⁹ conditions experienced at the LHC.
⁷²⁰

There are two main type of jet reconstruction used at CMS, Calorimeter (Calo) and Particle Flow (PF) jets [59]. Calorimeter jets are reconstructed using both the ECAL and HCAL cells, combined into calorimeter towers . These calorimeter towers consist of geometrically matched HCAL cells and ECAL crystals. Electronics noise is suppressed by applying a threshold to the calorimeter cells, with pile-up effects reduced by a requirement placed on the tower energy [60]. Calorimter jets are the jets used within the analyses described in this thesis.

PF jets are formed from combining information from all of the CMS subdetectors systems to determine which final state particles are present in the event. Generally, any particle is expected to produce some combination of a track in the silicon tracker, a deposit in the calorimeters, or a track in the muon system. The PF jet momentum and spatial resolutions are greatly improved with respect to calorimeter jets, as the use of the tracking detectors and of the high granularity of ECAL allows resolution and measurement of charged hadrons and photons inside a jet, which together constitute $\sim$ 85% of the jet energy [61].

The jets reconstructed by the clustering algorithm in CMS typically have an energy that differs to the 'true' energy measured by a perfect detector. This stems from the non-linear and nonuniform response of the calorimeters as well as other residual effects including pile-up and underlying events, and therefore additional corrections are applied to recover a uniform relative response as a function of pseudo-rapidity. These are applied as separate sub corrections [62].

- A PU correction is first applied to the jet. It subtracts the average extra energy deposited in the jet that comes from other vertices present in the event and is therefore not part of the hard jet itself.

- p_T and η dependant corrections derived from Monte Carlo simulations are used to account for the non-uniform response of the detector.

- p_T and η residual corrections are applied to data only to correct for difference between data and Monte Carlo. The residual is derived from QCD dijet samples and the p_T residual from $\gamma+$ jet and $Z+$ jets samples in data.

3.3.2. B-tagging

The decays of b quarks are suppressed by small CKM matrix elements. As a result, the lifetimes of b-flavoured hadrons, produced in the fragmentation of b quarks, are relatively long; $\mathcal{O}$ 1ps. The identification of jets origination from b quarks is very important for searches for new physics and for measurements of standard model processes.

Many different algorithms developed by CMS select b-quark jets based on variables such as the impact parameters of the charged-particle tracks, the properties of reconstructed decay vertices, and the presence or absence of a lepton, or combinations thereof. One of the most efficient of which is the Combined Secondary Vertex (CSV) which operates based on secondary vertex and track-based lifetime information, benchmarked in 'Loose', 'Medium' and 'Tight' working points, of which the medium point is the tagger used within the α_T search detailed in Section (4.1).

Using the CSV tagger, a likelihood-based discriminator distinguishes between jets from b-quarks, and those from charm or light quarks and gluons, which is shown in Figure 3.6. The minimum thresholds on the discriminator for each working point correspond to the misidentication probability for light-parton jets of 10%, 1%, and 0.1%, respectively, in jets with an average p_T of about 80 GeV.

The b-tagging performance is evaluated to measure the b-jet tagging efficiency ϵ_b, and the misidentification probability of charm ϵ_c and light-parton jets ϵ_s. The tagging efficiencies for each of these three jet flavours are compared between data and MC simulation, from which a series of p_T and $|\eta|$ binned jet corrections are determined,

$$SF_{b,c,s} = \frac{\epsilon_{b,c,s}^{data}}{\epsilon_{b,c,s}^{MC}}. \tag{3.2}$$

These are collectively named 'Btag Scale Factors' and allow MC simulation to accurately reflect the running conditions and performance of the tagging algorithm in data. Understanding of the b-tagging efficiency is essential in order to minimise systematic uncertainties in physics analyses that employ b-tagging.
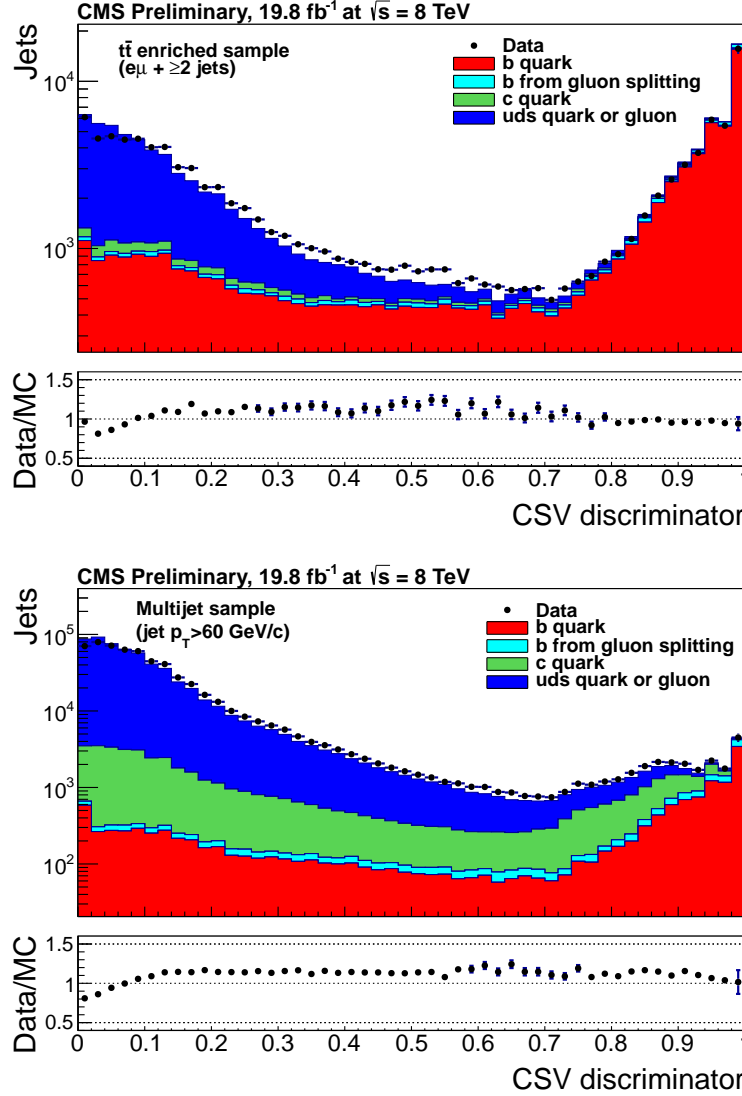
Figure 3.6.: CSV algorithm discriminator values in enriched ttbar (top) and inclusive multi jet samples (bottom) for b,c and light flavoured jets [63]. Working points are determined from the misidentification probability for light-parton jets to be tagged as a b-jet and are given as 0.244, 0.679 and 0.898 for L,M and T working points respectively.

The b-tagging efficiency is measured in data using several methods applied to multi jet events, primarily based on a sample of jets enriched in heavy flavour content. One method requires the collection of events with a soft muon within a cone $\Delta R < 0.4$ around the jet axis. Because the semileptonic branching fraction of b hadrons is significantly larger than that for other hadrons, these jets are more likely to arise from b quarks than from another flavour, with the resultant momentum component of the muon transverse to the jet axis larger for muons from b-hadron decays than from light or charm jets.

Additionally the performance of the tagger can also be benchmarked in $t\bar{t}$ events where in the SM, the top quark is expected to decay to a W boson and a b quark about 99.8% of the time [1]. Further selection criteria is applied to these events to further enrich the b quark content of these events. The methods to identify b-jets in data are discussed in great detail at [64]. The jet flavours are determined in simulation using truth level information and are compared to data to determine the correction scale factors (SF_b), which are displayed for the CSVM tagger in Figure 3.7.
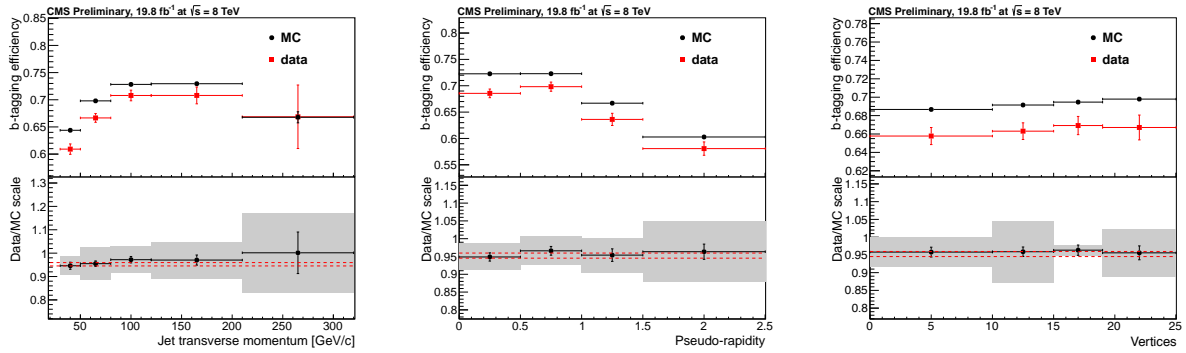

Figure 3.7.: Measured in $t\bar{t} \to$ di-lepton events using the CSVM tagger: (upper panels) b-tagging efficiencies and (lower panels) data/MC scale factor SF_b as a function of (left) jet p_T, (middle) jet $|\eta|$ and (right) number of primary vertices. In the lower panels, the grey filled areas represent the total statistical and systematic uncertainties, whereas the dotted lines are the average SF_b values within statistical uncertainties.

The measurement of the misidentication probability for light-parton jets relies on the inversion of tagging algorithms, selecting non-b jets using the same variables and techniques used in benchmarking the b-tagging efficiency. The scale factors (SF_s) to be applied to MC are shown in Figure 3.8 for the CSVM tagger.

3.4. Triggering System

With bunch crossings separated by just 25 ns, the rate at which data from all collisions would have to be written out and processed would be unfeasible. A two-tiered triggering system is applied at CMS in order to cope with the high collision rate of protons. The CMS trigger is designed to use limited information from each event to determine whether to record the event, reducing the rate of data taking to manageable levels whilst ensuring a high efficiency of interesting physics object events are selected.
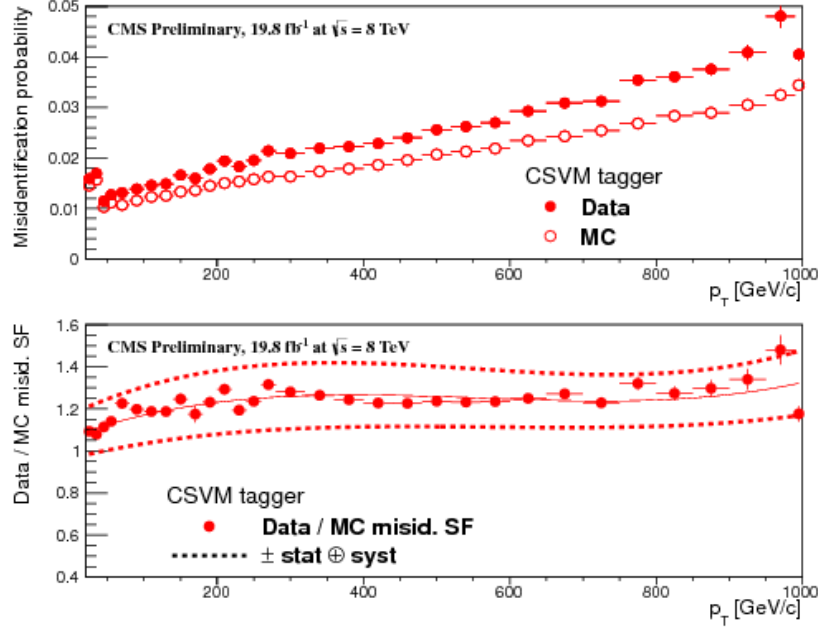
Figure 3.8.: For the CSVM tagging criterion: (top) misidentication probability in data (filled circles) and simulation (open circles); (bottom) scale factor for the misidentication probability. The last p_T bin in each plot includes all jets with $p_T > 1000$ GeV. The solid curve is the result of a polynomial fit to the data points. The dashed curves represent the overall statistical and systematic uncertainties on the measurements.

The L1 is a pipelined, dead-timeless system based on custom-built electronics [65], and is a combination of several sub systems which is shown pictorially in Figure 3.9. The L1 system is covered in more detail within the following section along with a description of the service work undertaken by the author to benchmark the performance of the L1 calorimeter trigger during the 2012 8 TeV run period.

The Higher Level Trigger (HLT) is a large farm of commercial computers [66]. The HLT processes events with software reconstruction algorithms that are more detailed, giving performance more similar to the reconstruction used offline. The HLT reduces the event rate written to disk by a factor of ~ 500 (~ 200Hz). The recorded events are transferred from CMS to the CERN computing centre, where event reconstruction is performed, and then distributed to CMS computing sites around the globe for storage and analysis.
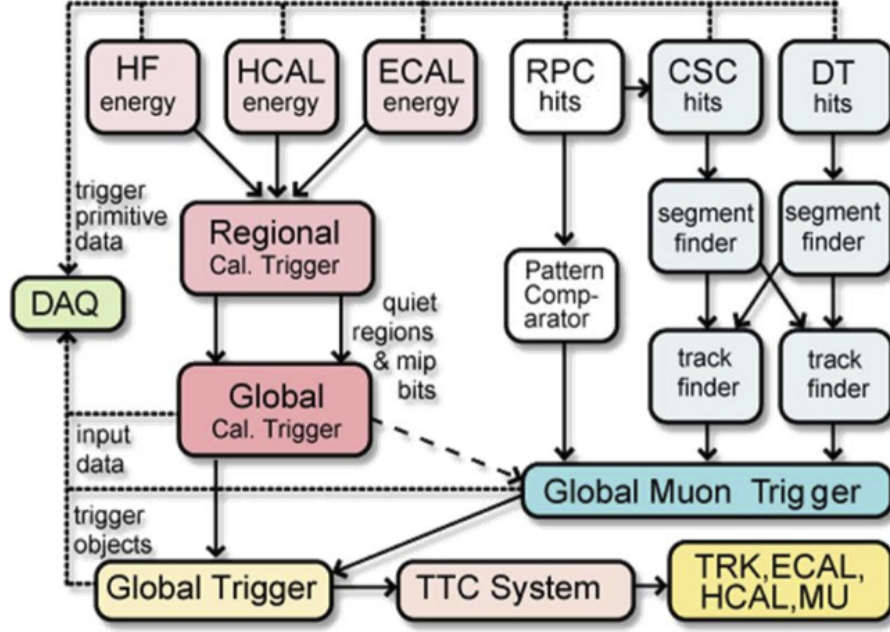
Figure 3.9.: The CMS L1 Trigger system.

3.4.1. The Level-1 Trigger

The L1 trigger reduces the rate of events collected from 40 MHz to ~ 100 kHz using information from the calorimeters and muon chambers, but not the tracker. A tree system of triggers is used to decide wether to pass on an event to the HLT for further reconstruction. Firstly the calorimeter and muon event information is kept separate, with local reconstruction of objects (μ,e,γ,jets) performed by the Regional Calorimeter Trigger (RCT) and Regional Muon Trigger (RMT) respectively. The RCT generates up to 72 isolated and non-isolated electromagnetic objects. These are sorted by rank, which is equivalent to transverse energy E_T, with the four highest ranked electromagnetic objects being passed via the Global Calorimeter Trigger (GCT) and Global MuonTrigger (GMT) to the Global Trigger (GT).

In the L1 GCT, coarse measurements of the energy deposited in the electromagnetic and hadronic calorimeters are combined and by using sophisticated algorithms the following physics objects are formed:

- isolated and non-isolated electromagnetic objects (e and γ);

- hadronic jets in the central and forward sections of the hadronic calorimeters;

- hadronically decaying tau leptons;

- total transverse energy (E_T), the scalar sum of the energy measured at L1, and missing transverse energy ($\not{E}_T$), defined as the vector sum of the energy of L1 objects;

- total transverse jet energy (H_T), the scalar sum of the energy of all L1 jet objects, and missing transverse jet energy ($\not{H}_T$), defined as the vector sum of the energy of L1 jets, are calculated from uncorrected L1 jets.

In addition quantities suitable for triggering minimum bias events, forward physics and beam background events are calculated. Additionally relevant muon isolation information is also passed on to the GMT for decisions involving the muon triggers where it is combined with information from across the three muon sub-systems. The resultant final accept/reject decision at L1 is then performed by the GT based on the objects received from the GCT and GMT (e/γ, μ, jets, E_T, $\not{E}_T$, H_T).

The L1 trigger is therefore of upmost importance to the functioning of the detector. Without a high-performing trigger and a good understanding of it's performance, there would be no data to analyse. Observations of how the L1 trigger performance is affected by changing LHC running conditions over the 2012 run period and also the introduction of a jet seed threshold to the L1 jet trigger algorithm is presented in the following Sections (3.4.2 - 3.4.6).

3.4.2. L1 Trigger Jet Algorithm

The L1 jet trigger uses the transverse energy sums computed in the calorimeter (both hadronic and electromagnetic) trigger regions. Each region consists of 4×4 trigger tower windows, spanning a region of $\Delta\eta \times \Delta\phi = 0.087 \times 0.087$ in pseudorapidity-azimuth. The jet trigger uses a 3×3 calorimeter region (112 trigger towers) sliding window technique which spans the full (η, ϕ) coverage of the CMS calorimeter as shown in Figure 3.10.

In forming a L1 jet is it required that the central region to be higher than the eight neighbouring regions $E_{Tcentral} > E_{Tsurround}$. Additionally a minimum threshold of 5 GeV on $E_{Tcentral}$ was introduced during the 2012 run period to suppress noise from pile-up, the effects of which are shown in Section (3.4.4).

The L1 jets are characterised by the E_T, summed over the 3×3 calorimeter regions, which corresponds to 12×12 trigger towers in barrel and endcap or 3×3 larger HF

861 towers in the HF. The ϕ size of the jet window is the same everywhere, whilst the η

862 binning gets somewhat larger at high η due to calorimeter and trigger tower segmentation.

863 The jets are labelled by (η, ϕ) indexes of the central calorimeter region.

864   Jets with $|\eta| > 3.0$ are classified as forward jets, whereas those with $|\eta| < 3.0$ are

865 classified as central. The four highest energy central, forward and τ jets in the calorimeter

866 are passed through Look Up Table (LUT)'s, which apply a programmable $\eta-$dependent

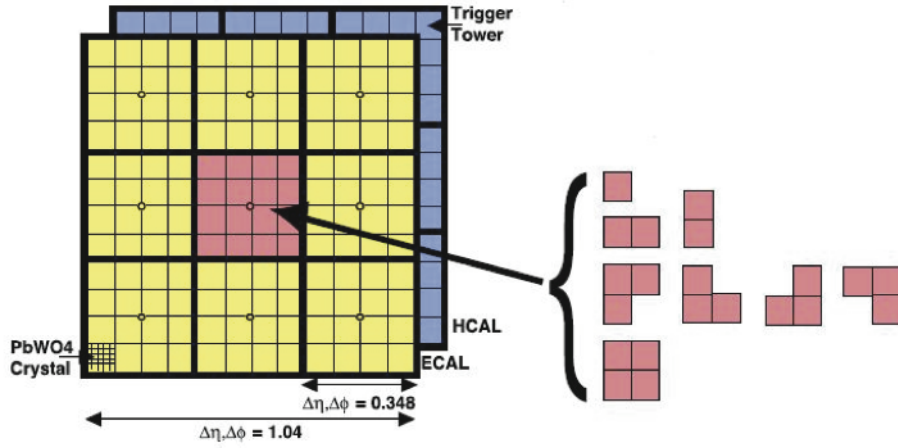867 jet energy scale correction. These are then used to make L1 trigger decisions.

Figure 3.10.: Illustration of the Level-1 jet finding algorithm.

868   The performance of the L1 jets is evaluated with respect to offline jets, which are

869 taken from the standard Calo jet and the PF jet reconstruction algorithms of CMS.

870 Jets are corrected for pile-up and detector effects as described in 3.3.1. A moderate

871 level of noise rejection is applied to the offline jets by selecting jets passing the "loose"

872 identification criteria for both Calo and PF. These criteria are summarised in Appendix

873 (A.1).

3.4.3. Measuring L1 Jet Trigger Efficiencies

875 The L1 jet efficiency is defined as the fraction of leading offline jets which were matched

876 with a L1 tau or central jet above a certain trigger threshold, divided by all the leading

877 offline jets in the event. This quantity is then plotted as a function of the offline jet E_T,

878 η and ϕ.

879   The efficiency is determined by matching the L1 and reconstructed offline jets spatially

880 in $\eta - \phi$ space. This is done by calculating the minimum separation in ΔR between the

highest offline reconstructed jet in E_T ($E_T > 10$ GeV, $|\eta| < 3$) and any L1 jet. A jet will be matched if this value is found to be < 0.5. Should more than one jet satisfy this, the jet closest in ΔR is taken as the matched jet. The matching efficiency is close to 100%, above ? 30(45) GeV for run 2012B(C) data (see Appendix (??)).

Each efficiency curve is fitted with a function which is the cumulative distribution function of an Exponentially Modified Gaussian (EMG) distribution:

$$f(x; \mu, \sigma, \lambda) = \frac{\lambda}{2} \cdot e^{\frac{\lambda}{2}(2\mu + \lambda\sigma^2 - 2x)} \cdot \text{erfc}(\frac{\mu + \lambda\sigma^2 - x}{\sqrt{2}\sigma}) \tag{3.3}$$

where erfc is the complementary error function defined as:

$$\text{erfc}(x) = 1 - \text{erf}(x) = \frac{2}{\sqrt{\pi}} \int_x^\infty e^{-t^2} dt.$$

In this functional form, the parameter μ determines the point of 50% of the plateau efficiency and the σ gives the resolution. This parametrisation is used to benchmark the efficiency at the plateau, the turn-on points and resolution for each L1 Jet trigger. The choice of function is purely empirical. Previous studies used the error function alone, which described the data well at high threshold values but could not describe the efficiencies well at lower thresholds [67].

The efficiency turn-on curves for various L1 jet thresholds are evaluated as a function of the offline reconstructed jet E_T for central jets with $|\eta| < 3$. These are measured using single isolated μ triggers which have high statistics, and are orthoganal and therefore unbiased to the hadronic triggers under study. The efficiency is calculated with respect to offline Calo and PF Jets in Figure 3.11. Table 3.1 shows the values of these parameters, calculated for three example L1 single jet triggers taken from 2012 8 TeV data.

The results from the L1 single jet triggers shows good performance for both Calo and PF jets. A better resolution for Calo jets with respect to L1 jets quantities is observed. This effect is due to Calo jet reconstruction using the same detector systems as in L1 jets, whereas with PF jet construction using tracker and muon information, a more smeared resolution when compared to L1 is expected.
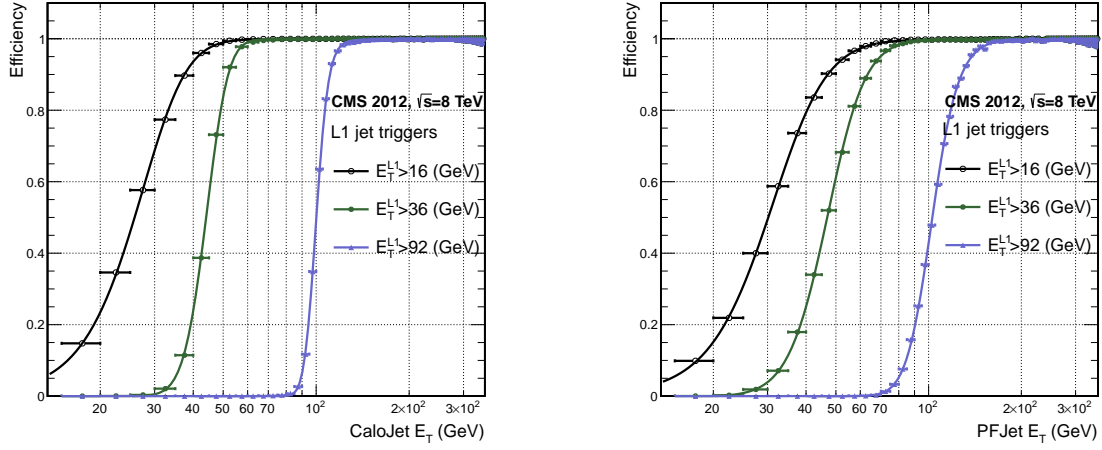
Figure 3.11.: L1 jet efficiency turn-on curves as a function of the offline CaloJet E_T (left) and PFJet E_T (right), measured in 2012 Run Period C data and collected with an isolated single μ data sample.

	Calo		PF	
Trigger	μ	σ	μ	σ
L1_SingleJet16	21.09 $\pm$ 0.03	7.01 $\pm$ 0.02	22.17 $\pm$ 0.04	7.83 $\pm$ 0.03
L1_SingleJet36	41.15 $\pm$ 0.05	5.11 $\pm$ 0.02	39.16 $\pm$ 0.06	8.04 $\pm$ 0.03
L1_SingleJet92	95.36 $\pm$ 0.13	5.62 $\pm$ 0.03	90.85 $\pm$ 0.19	11.30 $\pm$ 0.10

Table 3.1.: Results of a cumulative EMG function fit to the turn-on curves for L1 single jet triggers in run 2012 Run Period C, measured in an isolated μ data sample. The turn-on point, μ, and resolution, σ, of the L1 jet triggers are measured with respect to offline Calo Jets (left) and PF Jets (right).

3.4.4. Effects of the L1 Jet Seed

Between run period B and C of the 2012 data taking period, a jet seed threshold was introduced into the L1 trigger jet algorithm. There was previously no direct requirement made on the energy deposited in the central region. The introduction of a jet seed threshold required that the central region have $E_T \geq 5$GeV, and was introduced to counteract the effects of high pile up running conditions which create a large number of soft non-collimated jets, that are then added to the jets from the primary interaction or other soft jets from other secondary interactions [68]. This in turn causes a large increase in trigger rate due to the increase in the likelihood that the event causes the L1 trigger to fire. This was implemented to maintain trigger thresholds by cutting the rate of events recorded without significant reduction in the efficiency of physics events of interest.

916 The effect of the introduction of this jet seed threshold between these two run periods
917 is benchmarked through a comparison of the efficiency of the L1 jet triggers with respect
918 to offline Calo jets shown in Figure 3.12, and the L1 H_T trigger efficiency in Figure 3.14
919 which is compared to offline H_T constructed from Calo jets with $E_T \geq 40 \text{GeV}$.

920 To negate any effects from different pile-up conditions in the run periods, the efficiencies
921 are measured in events which contain between 15 and 20 primary vertices as defined in
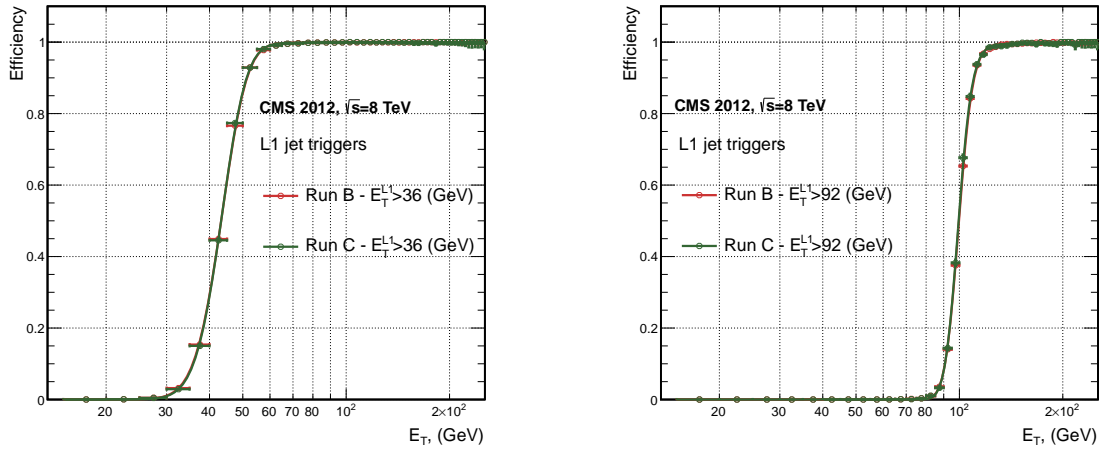922 Appendix (A.2).

Figure 3.12.: L1 jet efficiency turn-on curves as a function of the offline CaloJet E_T, measured for the L1 SingleJet 36 and 92 trigger in 2012 run period B and C collected with an isolated single μ' sample.

923 It can be seen that the performance of the $E_T > 36, 92$ single jet are almost identical,
924 with the jet seed having no measurable effect on these triggers as shown in Table 3.2 .

Trigger	2012B		2012C	
	μ	σ	μ	σ
L1_SingleJet36	40.29 $\pm$ 0.04	5.34 $\pm$ 0.02	40.29 $\pm$ 0.11	5.21 $\pm$ 0.05
L1_SingleJet92	94.99 $\pm$ 0.09	5.93 $\pm$ 0.06	94.82 $\pm$ 0.29	5.74 $\pm$ 0.18

Table 3.2.: Results of a cumulative EMG function fit to the turn-on curves for L1 single jet triggers in the 2012 run period B and C, preselected on an isolated muon trigger. The turn-on point μ and resolution σ of the L1 jet triggers are measured with respect to offline Calo Jets in run B (left) and run C (right).

925 For the H_T triggers, a large increase in rate during high pile-up conditions is expected.
926 This is due to the low energy threshold required for a jet to be added to the L1 H_T sum,

927 which is compiled from all uncorrected L1 jets formed in the RCT. The introduction
928 of the jet seed threshold removes the creation of many of these soft low E_T jets, thus
929 lowering the H_T calculation at L1. The effect on the trigger cross section for L1 H_T 150
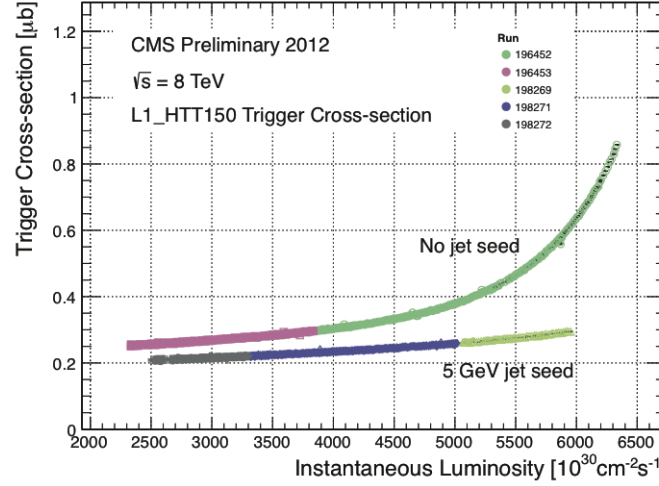930 trigger can be seen in Figure 3.13.

Figure 3.13.: Trigger cross section for the L1HTT150 trigger path. Showing that a 5 GeV
jet seed threshold dramatically reduces the dependance of cross section on the
instantaneous luminosity for L1 H_T triggers [69].

931 Different behaviours for the trigger turn ons between these run periods are therefore
932 expected. The turn on point is observed to shift to higher H_T values after the introduction
933 of the jet seed threshold, whilst having a sharper resolution due to less pile-up jets being
934 included the H_T sum, the results are shown in Table 3.3.

Trigger	2012B		2012C	
	μ	σ	μ	σ
L1 HT-100	157.5 $\pm$ 0.08	32.9 $\pm$ 0.08	169.8 $\pm$ 0.08	28.7 $\pm$ 0.03
L1 H1-150	230.9 $\pm$ 0.02	37.3 $\pm$ 0.01	246.4 $\pm$ 0.16	31.8 $\pm$ 0.05

Table 3.3.: Results of a cumulative EMG function fit to the turn-on curves for H_T in run
2012 B and C, preselected on an isolated single μ trigger. The turn-on point μ,
resolution σ of the L1 H_T triggers are measured with respect to offline H_T formed
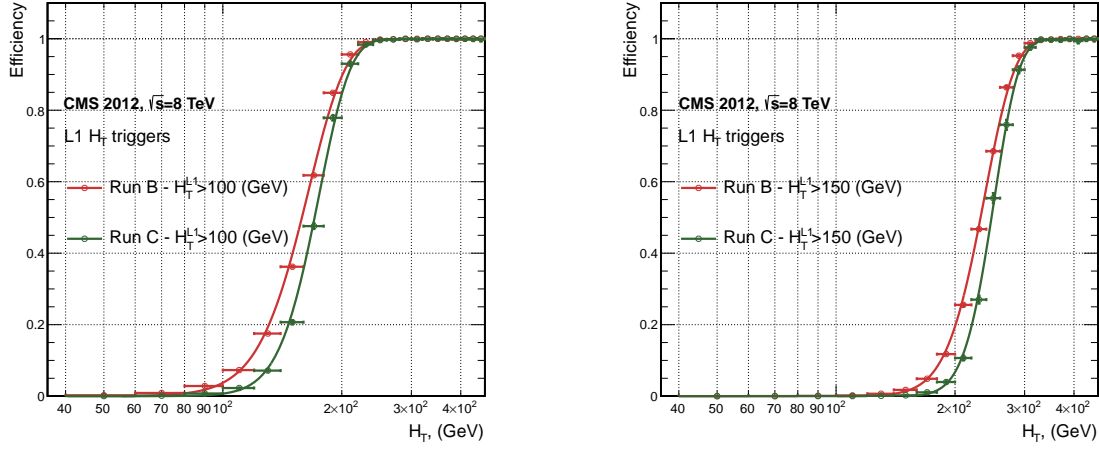from CaloJets with a $E_T \geq 40$ in run period B (left) and C (right).

Figure 3.14.: L1 H_T efficiency turn-on curves as a function of the offline CaloJet H_T, measured for the L1 H_T 100 and 150 trigger during the run 2012 B and C collected using an isolated single μ triggered sample.

3.4.5. Robustness of L1 Jet Performance against Pile-up

The performance of the L1 single jet triggers is evaluated in different pile-up conditions to benchmark any dependence on pile-up. Three different pile-up bins of 0-10, 10-20 and >20 vertices are defined, reflecting the low, medium and high pile-up running conditions at CMS in 2012. This is benchmarked relative to Calo and PF jets for the run 2012 C period where the jet seed threshold is applied, with L1 single jet thresholds of 16, 36 and 92 GeV, shown in Figure 3.15. The results of fits to these efficiency turn-on curves are given in Table 3.4 and Table 3.5 for Calo and PF jets respectively.

Vertices	0-10		11-20		> 20	
	μ	σ	μ	σ	μ	σ
L1_SingleJet16	19.9 $\pm$ 0.1	6.1 $\pm$ 0.3	20.8 $\pm$ 0.1	6.5 $\pm$ 0.1	22.3 $\pm$ 0.2	7.5 $\pm$ 0.1
L1_SingleJet36	41.8 $\pm$ 0.1	4.6 $\pm$ 0.1	40.9 $\pm$ 0.1	5.1 $\pm$ 0.1	40.6 $\pm$ 0.6	5.9 $\pm$ 0.2
L1_SingleJet92	95.9 $\pm$ 0.2	5.4 $\pm$ 0.1	95.2 $\pm$ 0.2	5.6 $\pm$ 0.1	94.5 $\pm$ 0.6	6.2 $\pm$ 0.3

Table 3.4.: Results of a cumulative EMG function fit to the efficiency turn-on curves for L1 single jet triggers in the 2012 run period C, measured from isolated μ triggered data. The turn-on point, μ, and resolution, σ, of the L1 jet triggers are measured with respect to offline Calo jets in low (left), medium (middle) and high (right) pile-up conditions.
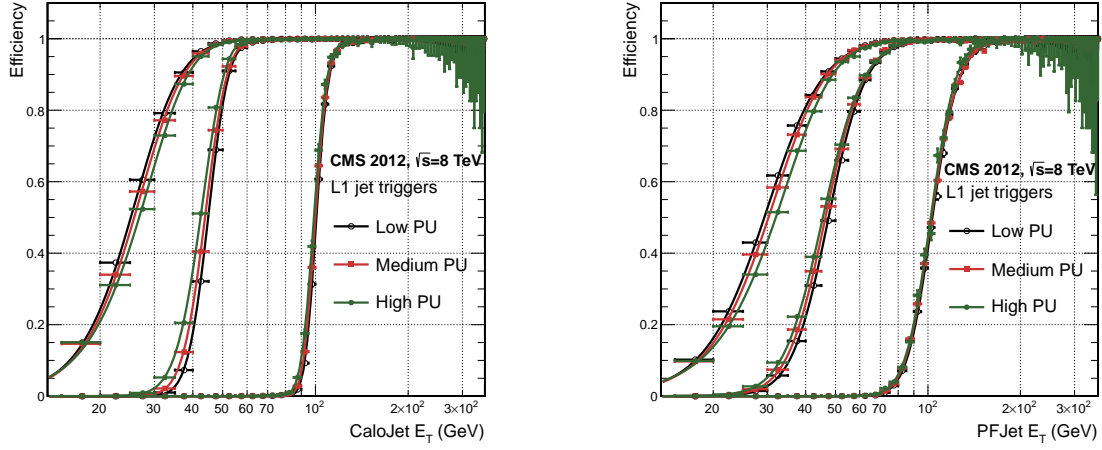
Figure 3.15.: L1 jet efficiency turn-on curves as a function of the leading offline E_T Calo (left) and PF (right) jet, for low, medium and high pile-up conditions.

Vertices	0-10		11-20		> 20	
	μ	σ	μ	σ	μ	σ
L1_SingleJet16	21.1 $\pm$ 0.1	7.16 $\pm$ 0.05	22.34 $\pm$ 0.1	7.9 $\pm$ 0.1	24.6 $\pm$ 0.2	9.5 $\pm$ 0.1
L1_SingleJet36	39.6 $\pm$ 0.1	7.4 $\pm$ 0.1	38.4 $\pm$ 0.1	7.4 $\pm$ 0.1	37.1 $\pm$ 0.2	7.5 $\pm$ 0.1
L1_SingleJet92	91.6 $\pm$ 0.3	11.3 $\pm$ 0.2	90.4 $\pm$ 0.3	11.2 $\pm$ 0.1	92.0 $\pm$ 0.9	12.1 $\pm$ 0.4

Table 3.5.: Results of a cumulative EMG function fit to the efficiency turn-on curves for Level-1 single jet triggers in the 2012 run period C, measured from isolated μ triggered data. The turn-on point, μ, and resolution, σ, of the L1 jet triggers are measured with respect to offline PF jets in low (left), medium (middle) and high (right) pile-up conditions.

No significant drop in efficiency is observed in the presence of a high number of primary vertices. The increase in hadronic activity in higher pile-up conditions, combined with the absence of pile-up subtraction for L1 jets, results in the expected observation of a decrease in the μ value of the efficiency turn-ons as a function of pile-up, while the resolution, σ of the turn-ons are found to gradually worsen as expected with increasing pile-up.

These features are further emphasised when shown as a function of

$$\frac{(\text{L1 E}_T - \text{Offline E}_T)}{\text{Offline E}_T} \tag{3.4}$$

in bins of matched leading offline jet E_T, of which the individual fits can be found in Appendix (B.2). Each of these distributions are fitted with an EMG function as defined in Equation (3.3).

The μ, σ and λ values extracted for the low, medium and high pile-up conditions are shown for Calo and PF jets in Figure 3.16 and Figure 3.17 respectively. The central value of $\frac{\text{(L1 } E_T - \text{Offline } E_T)}{\text{Offline } E_T}$ is observed to increases as a function of jet E_T, whilst the resolution is also observed to improve at higher offline jet E_T.
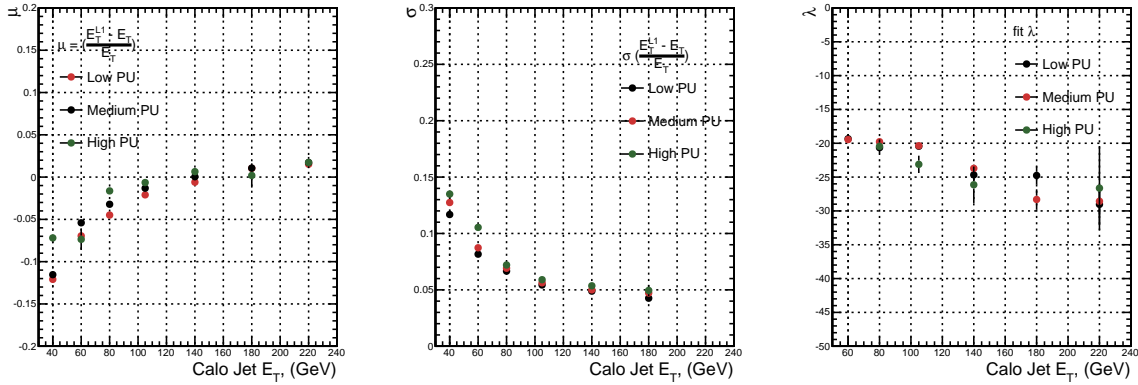
Figure 3.16.: Fit values from an EMG function fitted to the resolution plots of leading Calo jet E_T measured as a function of $\frac{\text{(L1 } E_T - \text{Offline } E_T)}{\text{Offline } E_T}$ for low, medium and high pile-up conditions. The plots show the mean μ (left), resolution σ (middle) of the Gaussian as well as the decay term λ (right) of the exponential.

The resolution of other L1 energy sum quantities, $\not{H}_T$, $\not{E}_T$ and $\sum E_T$ parameterised as in Equation (3.4), can be found in Appendix (B.3). The same behaviour observed for the single jet triggers is also found for these quantities, where in the presence of higher pile-up the μ values are shifted to higher values, with a worsening resolution, σ again due to the increase in soft pile-up jets and the absence of pile-up subtraction at L1.

3.4.6. Summary

The performance of the CMS Level-1 Trigger has been studied and evaluated for jets and energy sum quantities using data collected during the 2012 LHC 8TeV run. These studies include the effect of introduction of a 5 GeV jet seed threshold into the jet algorithm configuration, the purpose of which is to mitigate the effects of pile-up on the rate of L1 triggers whilst not adversely affecting the efficiency of these triggers. No significant
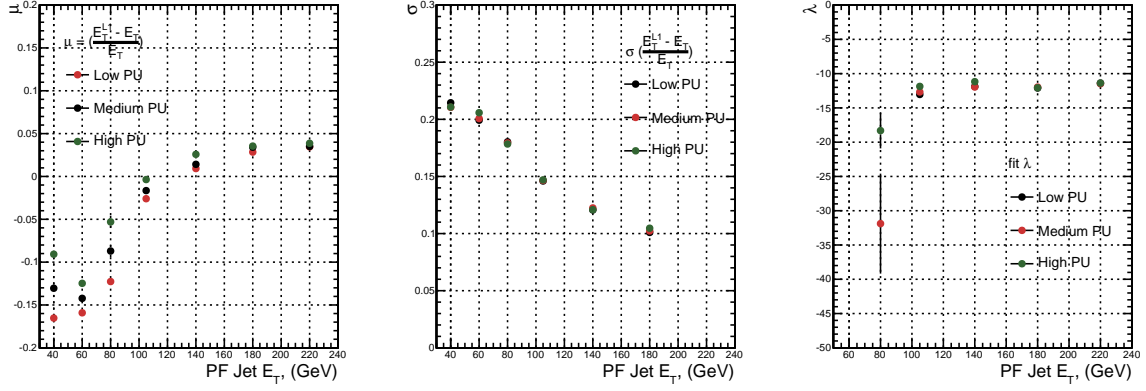
Figure 3.17.: Fit values from an EMG function fitted to the resolution plots of leading PF jet E_T measured as a function of $\frac{\text{(L1 } E_T - \text{Offline } E_T)}{\text{Offline } E_T}$ for low and medium pile-up conditions. The plots show the mean μ (left), resolution σ (middle) of the Gaussian as well as the decay term λ (right) of the exponential.

change in performance is observed with this change and good performance is observed for a range of L1 quantities.

Chapter 4.

Searches for SUSY in Hadronic Final States at the LHC

In this chapter a model independent search for SUSY in hadronic final states with $\not{E}_T$ using the α_T variable and b-quark multiplicity is introduced and described in detail. The results presented are based on a data sample of pp collisions collected in 2012 at $\sqrt{s} = 8$ TeV, corresponding to an integrate luminosity of 11.7 ± 0.5 fb^{-1}.

The kinematic variable α_T is motivated as a variable to provide strong rejections of QCD backgrounds, whilst maintaining sensitivity to possible a SUSY signal within Section (4.1). The search and trigger strategy in addition to the event reconstruction and selection are outlined within Sections (4.1.1-4.1.3).

The method in which the SM background is estimated using an analytical technique to improve statistical precision at higher b-tag multiplicities is detailed within Section (4.1.4), with a discussion on the impact of b-tagging and mis-tagging scale factors between data and MC on any background predictions. Finally a description of the formulation of appropriate systematic uncertainties applied to the background predictions to account for theoretical uncertainties and limitations in the simulation modelling of event kinematics and instrumental effects is covered in Section (4.1.5).

In addition to the α_T search, a complimentary technique is discussed as a means to predict the distribution of 3 and 4 reconstructed b-quark jets in an event in Section (4.2). The recent discovery of the Higgs boson has made third-generation "Natural SUSY" models attractive, given that light top and bottom squarks are a candidate to stabilise divergent loop corrections to the Higgs boson mass.

Using the α_T search as a base, a simple templated fit is employed to estimate the SM background in higher b-tag multiplicities (3-4) from a region of a low number of reconstructed b-jets (0-2). The predictions using this technique are first tested in simulation before being compared to the SM background predictions obtained from the α_T search.

4.1. The α_T search

The experimental signature of SUSY signal in the hadronic channel would manifest as a final state containing energetic jets and $\not{E}_T$. The search focuses on topologies where new heavy supersymmetric, R-parity conserving particles are pair-produced in pp collisions. These particles decaying to a LSP escape the detector undetected, leading to significant missing energy.

A search within this channel is greatly complicated in a hadron collider environment, where the overwhelming background comes from inherently balanced multi-jet ("QCD") events which are produced with an extremely large cross section. $\not{E}_T$ can appear in such events with a substation mis-measurement of jet energy or missed objects due to detector miscalibration or noise effects.

Additional SM background contribution comes from EWK processes with genuine $\not{E}_T$.

4.1.1. Search Strategy

4.1.2. Trigger Strategy

4.1.3. Event Selection

4.1.4. Background Estimation

4.1.5. Systematic Uncertainties on Transfer Factors

4.2. Searches for Natural SUSY with B-tag templates.

Btag Templates blah blah

Chapter 5.

Results

Results at 12fb 8TeV

5.1. Statistical Interpretation

Likelihood stuff

5.2. Interpretation in Simplified Signal Models

Result interpretation

Appendix A.

Miscellaneous

A.1. Noise Filters

For Calo jets the following criteria were applied:

- N90 hits > 1,

- HBHE > 0.01,

- fHPD < 0.98,

For PF jets the following criteria were applied:

- Neutral hadron fraction < 0.99,

- Neutral EM fraction < 0.99,

- Number of constituents > 1,

- Charged hadron fraction > 0,

- Charged multiplicity > 0,

- Charged EM fraction < 0.99.

The following noise filters are applied, to remove events with spurious, non-physical jets or missing transverse energy.

- CSC tight beam halo filter,

- HBHE noise filter with isolated noise rejection,

- HCAL laser filter,

- ECAL dead cell trigger primitive (TP) filter,

- Tracking failure filter,

- Bad EE Supercrystal filter,

- ECAL Laser correction filter.

A.2. Primary Vertices

The pileup per event is defined by the number of 'good' reconstructed primary vertices in the event, with each vertex satisfying the following requirements

- $N_{dof} > 4$;

- vertex position along the bead direction of $|z_{vtx}| < 24$cm;

- vertex position perpendicular to the beam of $\rho < 2$cm.

Appendix B.

L1 Jets

B.1. Jet matching efficiencies

The single jet turn-on curves are derived from events independent of wether the leading jet in an event is matched to a Level 1 jet using ΔR matching detailed in Section (3.4.3) or not. These turn-ons are produced from events which are not triggered on jet quantities and therefore it is not guaranteed that the lead jet of an event will be seeded by a Level 1 jet. Figure B.1 shows the particular matching efficiency of a lead jet to a L1 jet.
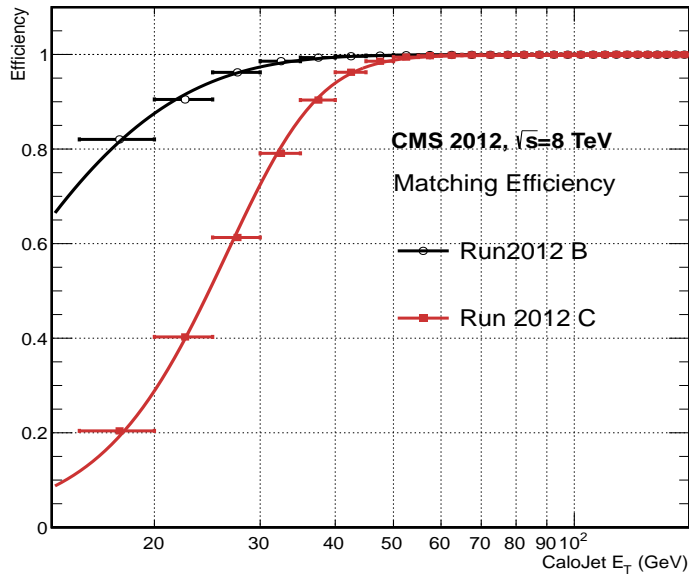

Figure B.1.: Leading jet matching efficiency as a function of the offline CaloJet E_T, measured in an isolated muon triggered dataset in the 2012B and 2012C run periods.

Run Period	μ	σ
2012B	6.62 $\pm$ 0.01	0.79 $\pm$ 0.03
2012C	19.51 $\pm$ 0.03	7.14 $\pm$ 0.02

Table B.1.: Results of a cumulative EMG function fit to the turn-on curves for the matching efficiency of the leading jet in an event to a Level-1 jet in run 2012C and 2012B data, measured in an isolated muon triggered sample. The turn-on point, μ, and resolution, σ, are measured with respect to offline Calo Jet E_T.

It can be seen that the turn on is sharper during the 2012B run period. The seed threshold requirement of a 5 GeV jet seed in run 2012C results in more events in which even the lead offline jet does not have an associated L1 jet. For larger jet E_T thresholds, typical of thresholds used in physics analyses, 100% efficiency is observed.

The matching efficiencies have a μ values of 6.62 GeV and 19.51 GeV for Run 2012B and 2012C respectively and is shown in Table B.1.
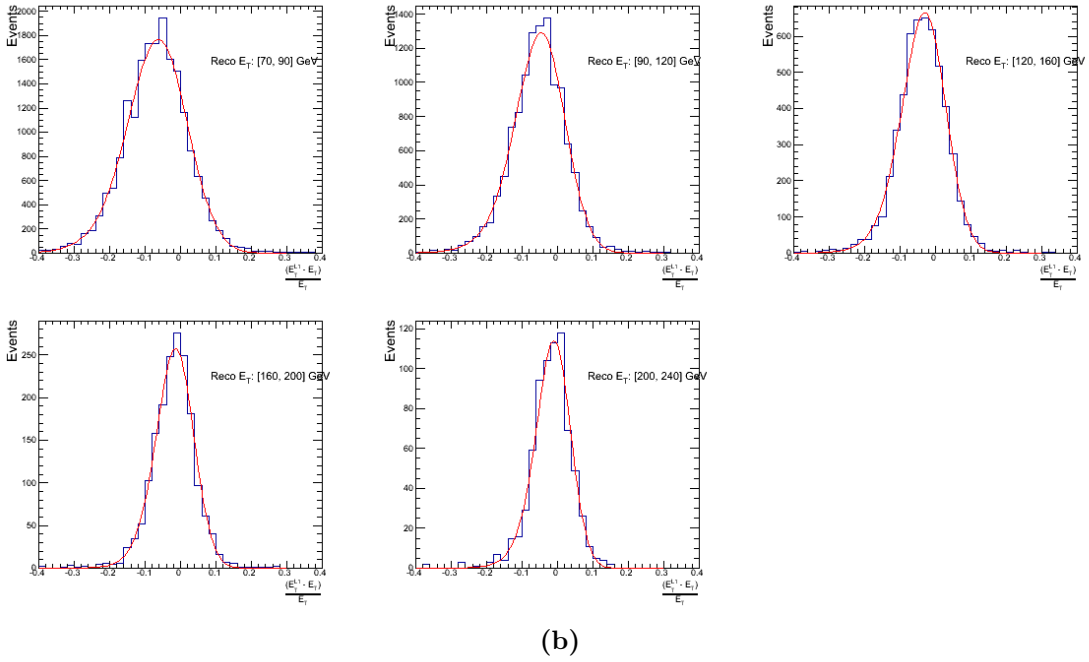
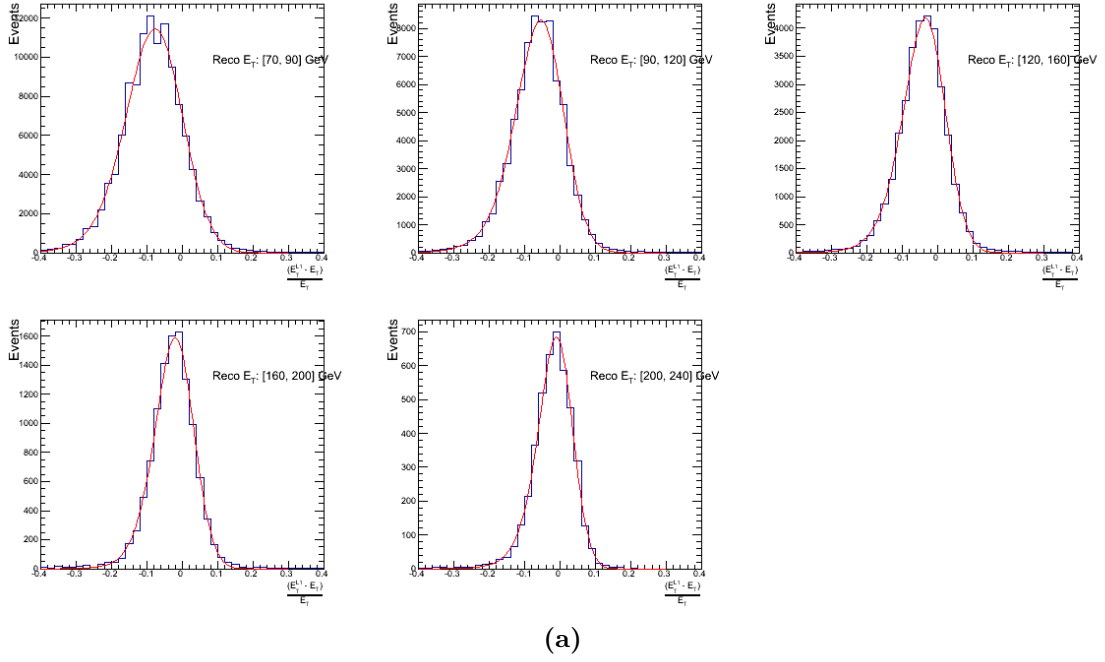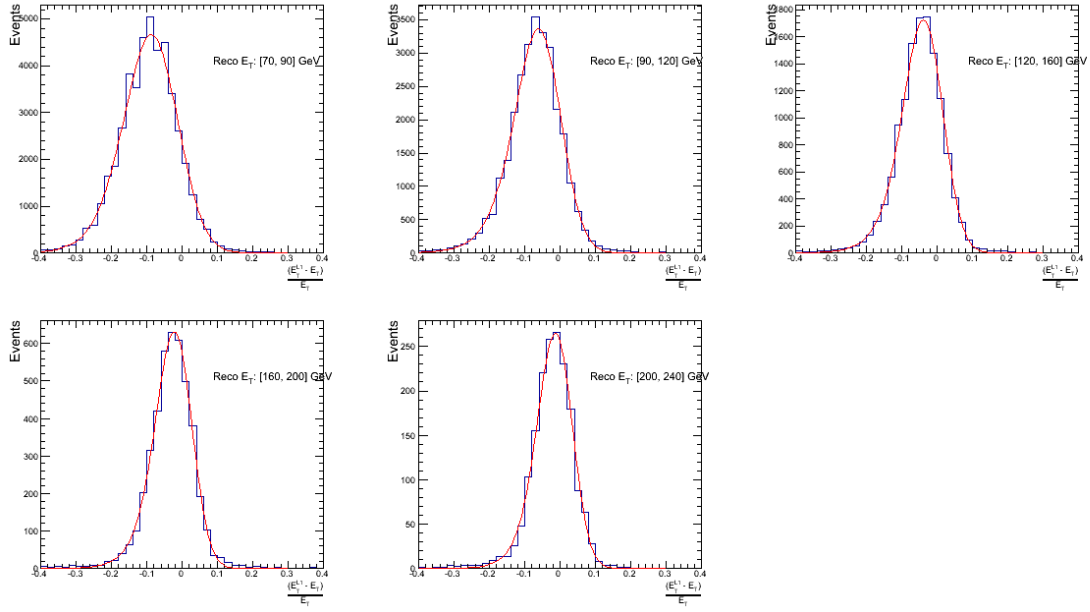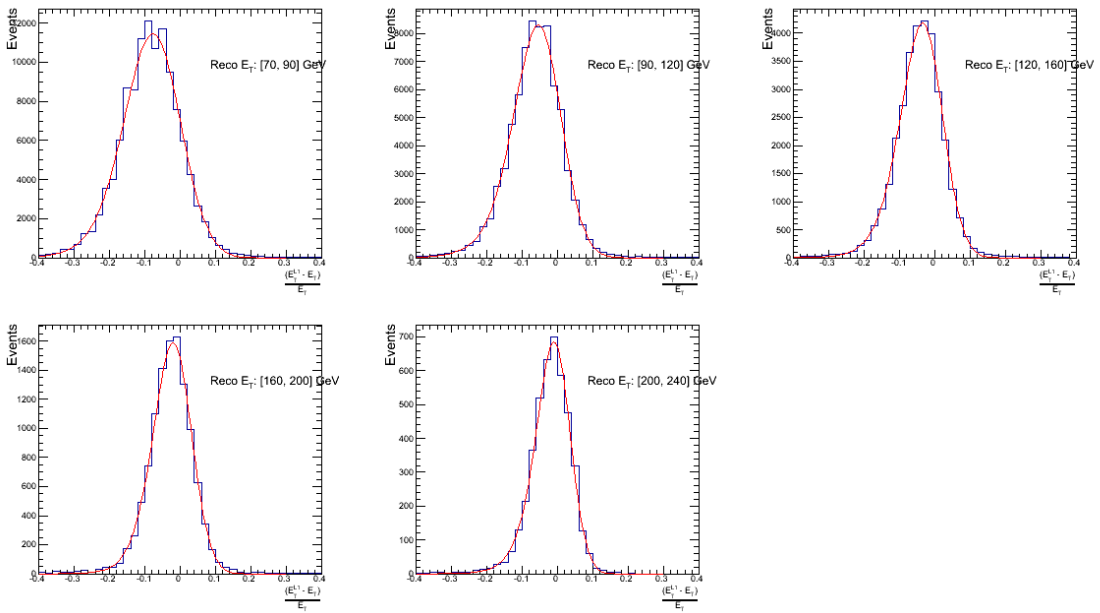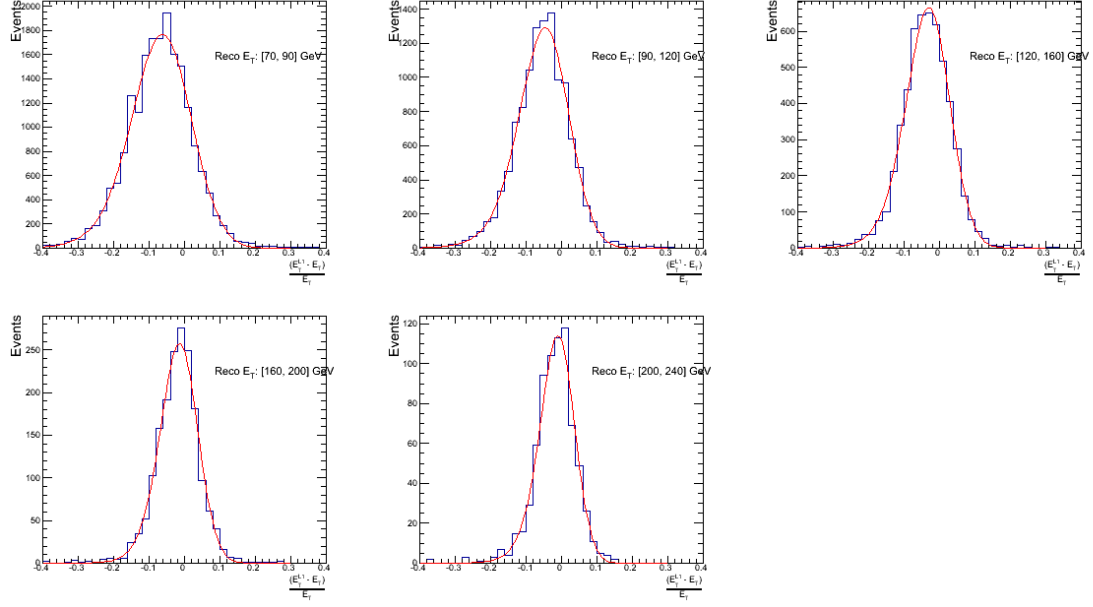## B.2. Leading Jet Energy Resolution

(a)

(a)

(b)
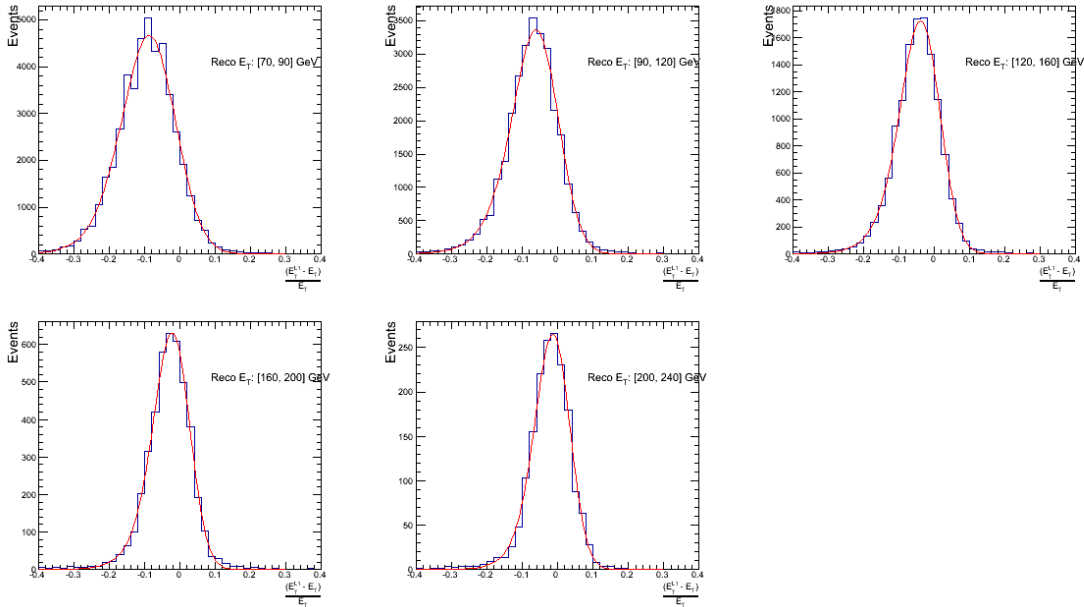
Figure B.2.: Resolution plots of the leading offline jet Calo E_T measured as a function of $\frac{(\text{L1 } E_T - \text{Offline } E_T)}{\text{Offline } E_T}$ for low (a), medium (b) and high (c) pile-up conditions.

(a)

(b)

(a)

Figure B.3.: Resolution plots of the leading offline jet PF E_T measured as a function of $\frac{(\text{L1 E}_T - \text{Offline E}_T)}{\text{Offline E}_T}$ for low (a), medium (b) and high (c) pile-up conditions.

B.3. Resolution for Energy Sum Quantities

The following plots show the resolution parameters for the four energy sum quantities as a function of the quantity (q) itself. In this case, The mean and RMS of the individual $\frac{(\text{L1 q} - \text{Offline q})}{\text{Offline q}}$ distributions, in bins of the quantity q is displayed.
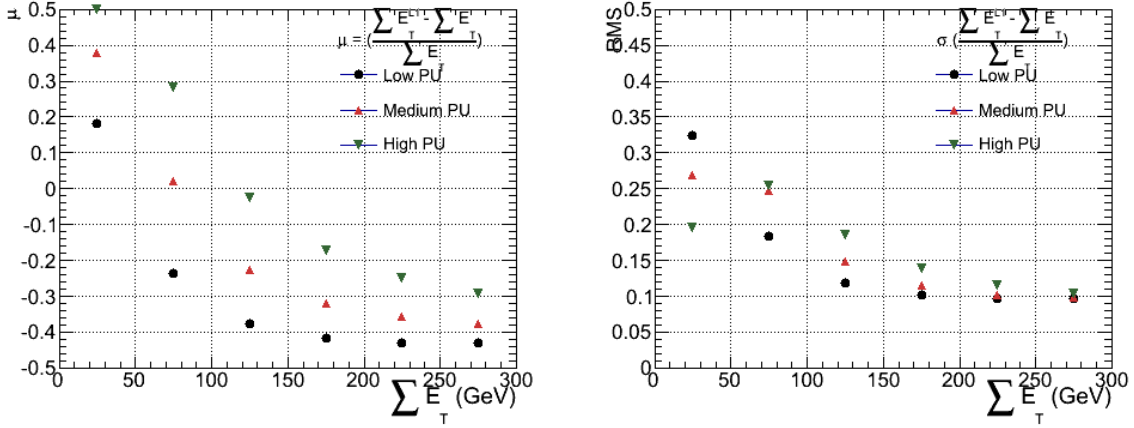
Figure B.4.: $\sum E_T$ resolution parameters in bins of Calo $\sum E_T$ measured for the defined low, medium and high pile up conditions. The plots show the mean μ (left), resolution σ (RMS) of the $\frac{\Delta q}{q}$ distributions.
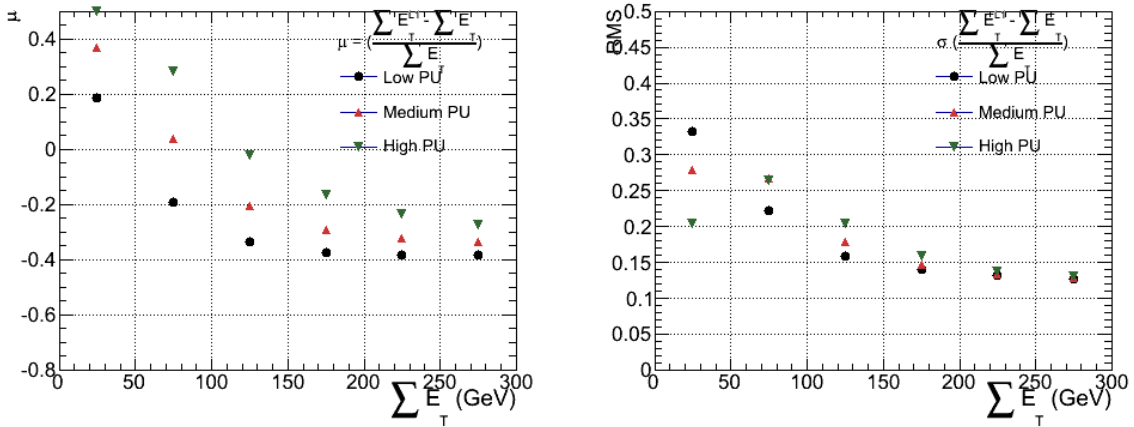

Figure B.5.: $\sum E_T$ resolution parameters in bins of PF $\sum E_T$ measured for the defined low, medium and high pile up conditions. The plots show the mean μ (left), resolution σ (RMS) of the $\frac{\Delta q}{q}$ distributions.
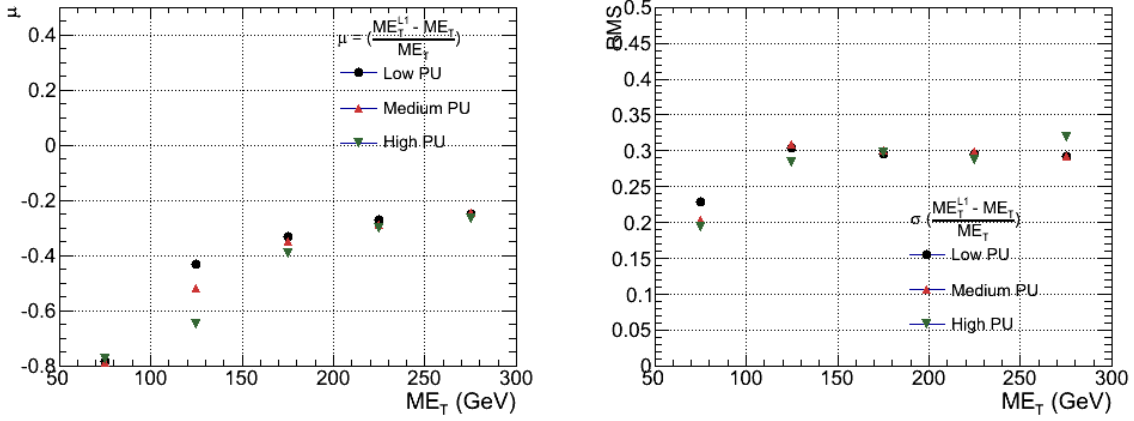
Figure B.6.: $\not{E}_T$ resolution parameters in bins of Calo $\not{E}_T$ measured for the defined low, medium and high pile up conditions. The plots show the mean μ (left), resolution σ (RMS) of the $\frac{\Delta q}{q}$ distributions.
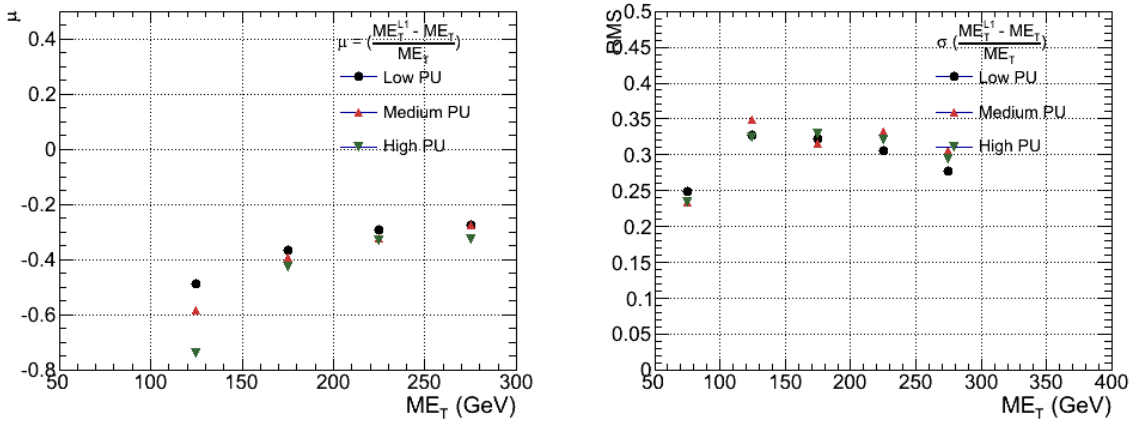

Figure B.7.: $\not{E}_T$ resolution parameters in bins of PF $\not{E}_T$ measured for the defined low, medium and high pile up conditions. The plots show the mean μ (left), resolution σ (RMS) of the $\frac{\Delta q}{q}$ distributions.

Figure B.8.: H_T resolution parameters in bins of Calo H_T measured for the defined low, medium and high pile up conditions. The plots show the mean μ (left), resolution σ (RMS) of the $\frac{\Delta q}{q}$ distributions.
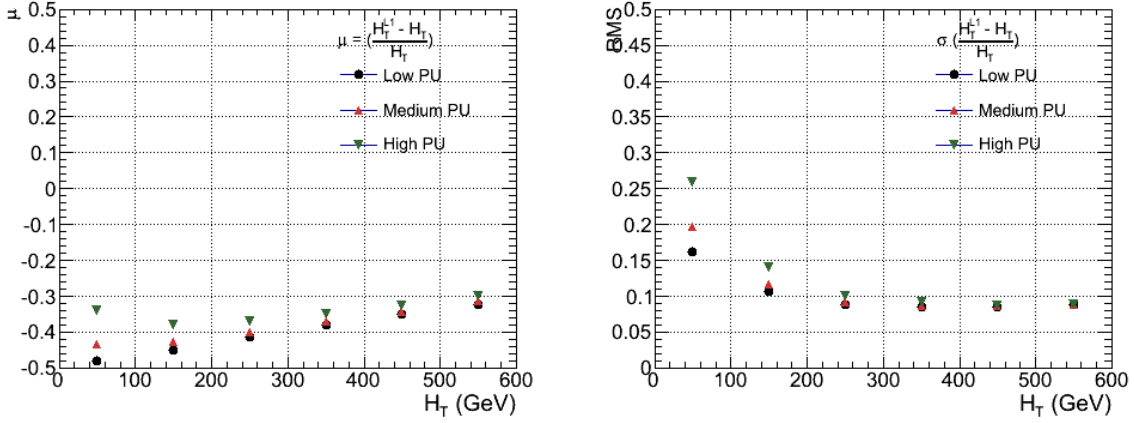

Figure B.9.: H_T resolution parameters in bins of PF H_T measured for the defined low, medium and high pile up conditions. The plots show the mean μ (left), resolution σ (RMS) of the $\frac{\Delta q}{q}$ distributions.

Figure B.10.: H_T resolution parameters in bins of H_T measured for the defined low, medium and high pile up conditions. The plots show the mean μ (left), resolution σ (RMS) of the $\frac{\Delta q}{q}$ distributions.
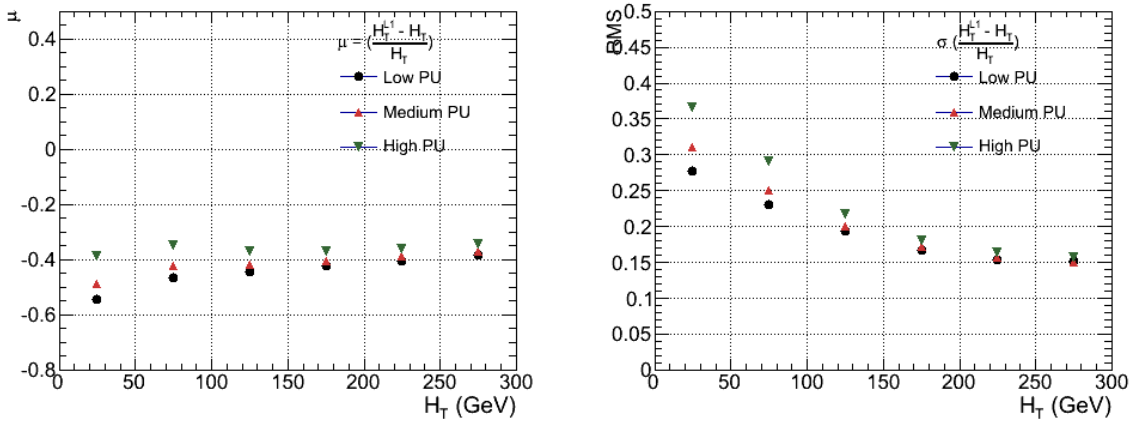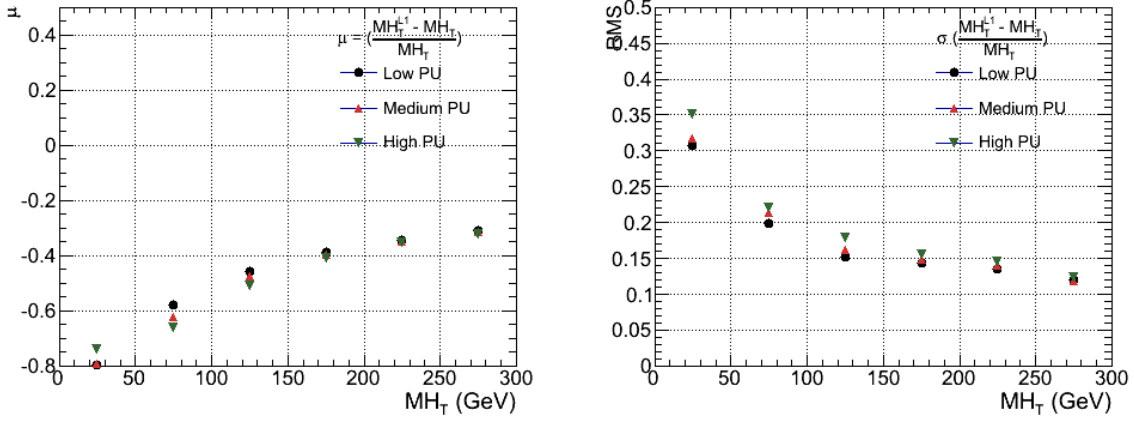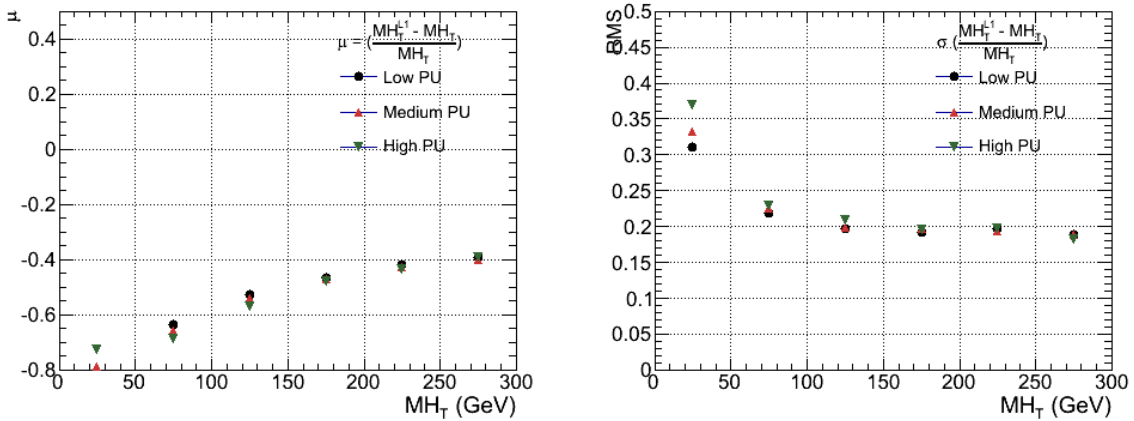

Figure B.11.: H_T resolution parameters in bins of PF H_T measured for the defined low, medium and high pile up conditions. The plots show the mean μ (left), resolution σ (RMS) of the $\frac{\Delta q}{q}$ distributions.

Bibliography

[1] J. Beringer *et al.*, "Review of Particle Physics (RPP)," *Phys.Rev.*, vol. D86, p. 010001, 2012.

[2] G. H. et al., "Nine-year wilkinson microwave anisotropy probe (wmap) observations: Cosmological parameter results," *The Astrophysical Journal Supplement Series*, vol. 208, no. 2, p. 19, 2013.

[3] G. Aad *et al.*, "Observation of a new particle in the search for the Standard Model Higgs boson with the ATLAS detector at the LHC," *Phys.Lett.*, vol. B716, pp. 1–29, 2012.

[4] S. Chatrchyan *et al.*, "Observation of a new boson at a mass of 125 GeV with the CMS experiment at the LHC," *Phys.Lett.*, vol. B716, pp. 30–61, 2012.

[5] S. Chatrchyan *et al.*, "Search for supersymmetry in hadronic final states with missing transverse energy using the variables AlphaT and b-quark multiplicity in pp collisions at 8 TeV," *Eur.Phys.J.*, vol. C73, p. 2568, 2013.

[6] S. Weinberg, "A model of leptons," *Phys. Rev. Lett.*, vol. 19, pp. 1264–1266, Nov 1967.

[7] S. Glashow, "Partial Symmetries of Weak Interactions," *Nucl.Phys.*, vol. 22, pp. 579–588, 1961.

[8] A. Salam, "Weak and Electromagnetic Interactions," *Conf.Proc.*, vol. C680519, pp. 367–377, 1968.

[9] G. Hooft, "Renormalizable lagrangians for massive yang-mills fields," *Nuclear Physics B*, vol. 35, no. 1, pp. 167 – 188, 1971.

[10] F. Hasert *et al.*, "Observation of Neutrino Like Interactions Without Muon Or Electron in the Gargamelle Neutrino Experiment," *Phys.Lett.*, vol. B46, pp. 138–140, 1973.

[11] G. Arnison *et al.*, "Experimental Observation of Lepton Pairs of Invariant Mass Around 95-GeV/c**2 at the CERN SPS Collider," *Phys.Lett.*, vol. B126, pp. 398–410, 1983.

[12] M. Banner *et al.*, "Observation of Single Isolated Electrons of High Transverse Momentum in Events with Missing Transverse Energy at the CERN anti-p p Collider," *Phys.Lett.*, vol. B122, pp. 476–485, 1983.

[13] E. Noether, "Invariante variationsprobleme," *Nachrichten von der Gesellschaft der Wissenschaften zu Gttingen, Mathematisch-Physikalische Klasse*, vol. 1918, pp. 235–257, 1918.

[14] F. Halzen and A. D. Martin, "Quarks and leptons." Wiley, 1985.

[15] *Introduction to Elementary Particles.* Wiley-VCH, 2nd ed., Oct. 2008.

[16] C. S. Wu, E. Ambler, R. W. Hayward, D. D. Hoppes, and R. P. Hudson, "Experimental Test of Parity Conservation in Beta Decay," *Physical Review*, vol. 105, pp. 1413–1415, Feb. 1957.

[17] P. Higgs, "Broken symmetries, massless particles and gauge fields," *Physics Letters*, vol. 12, no. 2, pp. 132 – 133, 1964.

[18] F. Englert and R. Brout, "Broken symmetry and the mass of gauge vector mesons," *Phys. Rev. Lett.*, vol. 13, pp. 321–323, Aug 1964.

[19] P. W. Higgs, "Broken symmetries and the masses of gauge bosons," *Phys. Rev. Lett.*, vol. 13, pp. 508–509, Oct 1964.

[20] G. S. Guralnik, C. R. Hagen, and T. W. B. Kibble, "Global conservation laws and massless particles," *Phys. Rev. Lett.*, vol. 13, pp. 585–587, Nov 1964.

[21] S. Weinberg, "A model of leptons," *Phys. Rev. Lett.*, vol. 19, pp. 1264–1266, Nov 1967.

[22] H. Yukawa, "On the interaction of elementary particles. i," *Progress of Theoretical Physics Supplement*, vol. 1, pp. 1–10, 1955.

[23] Y. e. a. Fukuda, "Evidence for oscillation of atmospheric neutrinos," *Phys. Rev. Lett.*, vol. 81, pp. 1562–1567, Aug 1998.

[24] R. Becker-Szendy, C. Bratton, D. Casper, S. Dye, W. Gajewski, *et al.*, "A Search for muon-neutrino oscillations with the IMB detector," *Phys.Rev.Lett.*, vol. 69,

pp. 1010–1013, 1992.

[25] S. P. Martin, "A Supersymmetry primer," 1997.

[26] H. Nilles, *Supersymmetry, Supergravity and Particle Physics*. Physics reports, North-Holland Physics Publ., 1984.

[27] H. E. Haber and G. L. Kane, "The Search for Supersymmetry: Probing Physics Beyond the Standard Model," *Phys.Rept.*, vol. 117, pp. 75–263, 1985.

[28] E. Witten, "Dynamical Breaking of Supersymmetry," *Nucl.Phys.*, vol. B188, p. 513, 1981.

[29] J. Wess and B. Zumino, "Supergauge transformations in four dimensions," *Nuclear Physics B*, vol. 70, no. 1, pp. 39 – 50, 1974.

[30] H. Muller-Kirsten and A. Wiedemann, *Introduction to Supersymmetry*. World Scientific lecture notes in physics, World Scientific, 2010.

[31] I. Aitchison, *Supersymmetry in Particle Physics: An Elementary Introduction*. Cambridge University Press, 2007.

[32] K. A. Intriligator and N. Seiberg, "Lectures on Supersymmetry Breaking," *Class.Quant.Grav.*, vol. 24, pp. S741–S772, 2007.

[33] Y. Shadmi, "Supersymmetry breaking," pp. 147–180, 2006.

[34] C. Burgess, P. G. Camara, S. de Alwis, S. Giddings, A. Maharana, *et al.*, "Warped Supersymmetry Breaking," *JHEP*, vol. 0804, p. 053, 2008.

[35] H. Murayama, "Supersymmetry breaking made easy, viable, and generic," 2007.

[36] H. Baer and X. Tata, *Weak Scale Supersymmetry: From Superfields to Scattering Events*. Cambridge University Press, 2006.

[37] S. P. Martin, "Implications of supersymmetric models with natural r-parity conservation," 1996.

[38] G. L. Kane, C. F. Kolda, L. Roszkowski, and J. D. Wells, "Study of constrained minimal supersymmetry," *Phys.Rev.*, vol. D49, pp. 6173–6210, 1994.

[39] C. Strege, G. Bertone, D. Cerdeno, M. Fornasa, R. Ruiz de Austri, *et al.*, "Updated global fits of the cMSSM including the latest LHC SUSY and Higgs searches and XENON100 data," *JCAP*, vol. 1203, p. 030, 2012.

[40] M. Citron, J. Ellis, F. Luo, J. Marrouche, K. Olive, *et al.*, "The End of the CMSSM Coannihilation Strip is Nigh," *Phys.Rev.*, vol. D87, p. 036012, 2013.

[41] D. Ghosh, M. Guchait, S. Raychaudhuri, and D. Sengupta, "How Constrained is the cMSSM?," *Phys.Rev.*, vol. D86, p. 055007, 2012.

[42] D. Alves *et al.*, "Simplified Models for LHC New Physics Searches," *J.Phys.*, vol. G39, p. 105005, 2012.

[43] J. Alwall, P. Schuster, and N. Toro, "Simplified Models for a First Characterization of New Physics at the LHC," *Phys.Rev.*, vol. D79, p. 075020, 2009.

[44] S. Chatrchyan *et al.*, "Interpretation of Searches for Supersymmetry with simplified Models," *Phys.Rev.*, vol. D88, p. 052017, 2013.

[45] J. Hisano, K. Kurosawa, and Y. Nomura, "Natural effective supersymmetry," *Nucl.Phys.*, vol. B584, pp. 3–45, 2000.

[46] M. Papucci, J. T. Ruderman, and A. Weiler, "Natural SUSY Endures," *JHEP*, vol. 1209, p. 035, 2012.

[47] B. Allanach and B. Gripaios, "Hide and Seek With Natural Supersymmetry at the LHC," *JHEP*, vol. 1205, p. 062, 2012.

[48] K. Aamodt *et al.*, "The ALICE experiment at the CERN LHC," *JINST*, vol. 3, p. S08002, 2008.

[49] G. Aad *et al.*, "The ATLAS Experiment at the CERN Large Hadron Collider," *JINST*, vol. 3, 2008.

[50] R. Adolphi *et al.*, "The cms experiment at the cern lhc," *JINST*, vol. 0803, p. S08004, 2008.

[51] A. A. Alves *et al.*, "The LHCb Detector at the LHC," *JINST*, vol. 3, p. S08005, 2008.

[52] J.-L. Caron, "Lhc layout.. schema general du lhc.." Sep 1997.

[53] C. Collaboration, "Cms luminosity - public results." twiki.cern.ch/twiki/bin/view/CMSPublic/LumiPublicResults., 2011.

[54] CERN, "Cms compact muon solenoid.." http://public.web.cern.ch/public/Objects/LHC/CMSnc.jpg Feb 2010.

[55] *The CMS electromagnetic calorimeter project: Technical Design Report.* Technical Design Report CMS, Geneva: CERN, 1997.

[56] *The CMS muon project: Technical Design Report.* Technical Design Report CMS, Geneva: CERN, 1997.

[57] CMS Collaboration, "The cms physics technical design report, volume 1," *CERN/LHCC*, vol. 2006-001, 2006.

[58] M. Cacciari, G. P. Salam, and G. Soyez, "The anti- k t jet clustering algorithm," *Journal of High Energy Physics*, vol. 2008, no. 04, p. 063, 2008.

[59] "Jet performance in pp collisions at 7 tev," Tech. Rep. CMS-PAS-JME-10-003, CERN, Geneva, 2010.

[60] X. Janssen, "Underlying event and jet reconstruction in cms," Tech. Rep. CMS-CR-2011-012, CERN, Geneva, Jan 2011.

[61] T. C. collaboration, "Determination of jet energy calibration and transverse momentum resolution in cms," *Journal of Instrumentation*, vol. 6, no. 11, p. P11002, 2011.

[62] R. Eusebi and on behalf of the CMS collaboration), "Jet energy corrections and uncertainties in cms: reducing their impact on physics measurements," *Journal of Physics: Conference Series*, vol. 404, no. 1, p. 012014, 2012.

[63] "Performance of b tagging at sqrt(s)=8 tev in multijet, ttbar and boosted topology events," no. CMS-PAS-BTV-13-001, 2013.

[64] T. C. collaboration, "Identification of b-quark jets with the cms experiment," *Journal of Instrumentation*, vol. 8, no. 04, p. P04013, 2013.

[65] S. Dasu *et al.*, "CMS. The TriDAS project. Technical design report, vol. 1: The trigger systems," 2000.

[66] P. Sphicas, "CMS: The TriDAS project. Technical design report, Vol. 2: Data acquisition and high-level trigger," 2002.

[67] J. B. et al., " Calibration and Performance of the Jets and Energy Sums in the Level-1 Trigger ," no. CMS IN 2013/006 (2013), 2013.

[68] B. et al., " Study of Level-1 Trigger Jet Performance in High Pile-up Running Conditions," no. CMS IN 2013/007 (2013), 2013.

[69] J. J. Brooke, "Performance of the cms level-1 trigger," Tech. Rep. CMS-CR-2012-322. CERN-CMS-CR-2012-322, CERN, Geneva, Nov 2012.

Acronyms

ALICE   A Large Ion Collider Experiment

ATLAS   A Toroidal LHC ApparatuS

APD   Avalanche Photo-Diodes

BSM   Beyond Standard Model

CERN   European Organization for Nuclear Research

CMS   Compact Muon Solenoid

CMSSM   Compressed Minimal SuperSymmetric Model

CSC   Cathode Stripe Chamber

CSV   Combined Secondary Vertex

CSVM   Combined Secondary Vertex Medium Working Point

DT   Drift Tube

ECAL   Electromagnetic CALorimeter

EB   Electromagnetic CALorimeter Barrel

EE   Electromagnetic CALorimeter Endcap

ES   Electromagnetic CALorimeter pre-Shower

EMG   Exponentially Modified Gaussian

EPJC   European Physical Journal C

EWK   Electroweak Sector

GCT   Global Calorimeter Trigger

GMT   Global MuonTrigger

GT   Global Trigger

HB   Hadron Barrel

HE   Hadron Endcaps

1241	**HF**	Hadron Forward
1242	**HO**	Hadron Outer
1243	**HCAL**	Hadronic CALorimeter
1244	**HLT**	Higher Level Trigger
1245	**LUT**	Look Up Table
1246	**L1**	Level 1 Trigger
1247	**LHC**	Large Hadron Collider
1248	**LHCb**	Large Hadron Collider Beauty
1249	**LSP**	Lightest Supersymmetric Partner
1250	**PS**	Proton Synchrotron
1251	**QED**	Quantum Electro-Dynamics
1252	**QCD**	Quantum Chromo-Dynamics
1253	**QFT**	Quantum Field Theory
1254	**RPC**	Resistive Plate Chamber
1255	**RCT**	Regional Calorimeter Trigger
1256	**RMT**	Regional Muon Trigger
1257	**SUSY**	SUperSYmmetry
1258	**SM**	Standard Model
1259	**SMS**	Simplified Model Spectra
1260	**SPS**	Super Proton Synchrotron
1261	**VEV**	Vacuum Expectation Value
1262	**VPT**	Vacuum Photo-Triodes
1263	**WIMP**	Weakly Interacting Massive Particle